Dynamics and Evolution of a Giant Solar Filament as Observed by the Solar Dynamics Observatory

Bachelorarbeit
in der Wissenschaftsdisziplin Physik

eingereicht an der
Mathematisch-Naturwissenschaftlichen Fakultät
der Universität Potsdam

Erstgutachter und Betreuer: apl. Prof. Dr. Carsten Denker
Zweitgutachter: apl. Prof. Dr. Gottfried Mann

Andrea Diercke

27 March 2014

Leibniz-Institut für Astrophysik Potsdam
An der Sternwarte 16
14482 Potsdam

Universität Potsdam, Campus Golm
Institut für Physik und Astronomie (Haus 28)
Karl-Liebknecht-Strasse 24/25
14476 Potsdam-Golm

Table of Contents

Abstract

Space-weather effects can negatively impact our technical society by disturbing GPS signals, causing geomagnetically induced currents, which damage power grids, or enhancing the radiation exposure of airplane passengers and crew on polar routes. Therefore, it is important to know the origins of these disturbances, in particular those of coronal mass ejections (CMEs). One source of CMEs are filament eruptions. In this thesis, I study the dynamics and evolution of a giant solar filament located in the northern hemisphere of the Sun, which covered around one third of the solar diameter. Such an enormous quiet-Sun filament is a rare phenomenon and only few examples have been reported in literature. A filament is a cloud of cold plasma in the chromosphere reaching up into the corona. Because of the temperature differences between filament and coronal plasma and due to absorbing photospheric radiation filaments appear as dark structures on the solar disk. Observed above the limb, filaments appear in emission as loops and are called prominences.

To analyze the filament, I use the data of two instruments on board the Solar Dynamics Observatory (SDO), i.e., the Atmospheric Imaging Assembly (AIA) and the Helioseismic and Magnetic Imager (HMI). Extreme ultraviolet (EUV) images of AIA cover five different wavelength bands and HMI provides the continuum images and magnetograms. I downloaded and processed the data with the help of the SolarSoft library (SSW) implemented in the Interactive Data Language (IDL). I define a region-of-interest (ROI) of 1088 Mm$\times$384 Mm around the filament, select a reference time and apply a differential rotation correction to align the time-series. Furthermore, I apply geometric corrections to remove projection effects and to resample the images onto an equidistant grid.

I have two kinds of data sets: a long-duration and a high-cadence data set. The first has a duration from the 8–22 November 2011 with a time cadence of one hour. The latter has a duration of two hours on 16 November 2011 from 11:00 to 13:00 UT, when the Sun's central meridian intersects the filament in the middle. The time cadence in this data set differs: the AIA wavelength bands 171 Å, 193 Å, 211 Å, and 304 Å have a time cadence of 12 s, the AIA 1600 Å wavelength band has a time cadence of 24 s, and the HMI magnetograms and continuum images have a time cadence of 45 s.

I use the long-duration data set to analyze the evolution of the filament. The different wavelength bands allow me to have a look at different layers of the solar atmosphere from the photosphere, via the chromosphere to the corona. Two eruptions appeared while the filament was visible on the Sun. With the last eruption the filament vanished from the solar surface as a CME. Additionally, I determine the chirality of the filament. The filament is a dextral one, which is very typical in the northern hemisphere. This provides the information about the helicity of the filament. Furthermore, I create so-called tricolor images, which are a composition of three different, temperature-sensitive spectral lines originating in different layers of the corona. The colors of the image correspond to our perception of temperatures.

I use the high-cadence data set to analyze the dynamics of the filament. First, I create a deep magnetogram to enhance the fine structure of the magnetic field. Additionally, I measure the magnetic flux transport velocity, which I compare with velocity measurements of optical flows in chromosphere and corona. For this purpose, I use two different algorithms. To measure the flux transport velocities, I use the differential affine velocity estimator (DAVE), which exploits the spatial and temporal derivatives of the magnetograms to compute the velocities. Here, I study how the velocity depends on the duration of the time-series and time interval used for the temporal derivatives. To compute the velocities in the photosphere and chromosphere, I use local correlation tracking (LCT), which computes local cross-correlations between successive images of a time-series. Finally, a new technique for image enhancement, the noise adaptive fuzzy equalization (NAFE) method, is used to improve contrast of the AIA 171 Å images. This new method allows to discover counter-streaming flows of coronal plasma inside the filament's spine. In addition, I use LCT to compute the velocities based on EUV images. Furthermore, I determine the dependence of the flow fields in a small region on the time period over which the flow maps are averaged. To determine the counter-streaming flows, I study a region of 32 Mm$\times$32 Mm and make a azimuth map to display the direction of the flows. It is possible to identify the counter-streaming in flow maps and the azimuth maps over 15- and 90-minute duration.

Zusammenfassung

Die Auswirkungen des Weltraumwetters sind auf negative Weise in unserer technischen Gesellschaft spürbar. So werden beispielsweise GPS-Signale gestört, geomagnetische Ströme induziert, welche die Stromleitungen beschädigen können, oder es werden erhöhte Strahlungsdosen bei Passagieren und Crewmitgliedern von Flugzeugen auf polaren Routen festgestellt. Daher ist es wichtig die Ursprünge von solchen Ereignissen näher zu untersuchen, im Besondern die von Koronalen Massenauswürfen (CMEs). Eine Quelle von CMEs sind Filamenteruptionen. In dieser Arbeit habe ich die Dynamik und die zeitliche Entwicklung eines gigantischen Sonnenfilaments auf der nördlichen Hemisphäre untersucht, welches etwa ein Drittel des Sonnendurchmessers ausgemacht hat. Solch ein großes Filament auf der ruhigen Sonne ist ein sehr seltenes Ereignis und ist dem entsprechend kaum untersucht. Ein Filament ist eine Wolke aus relativ kaltem Plasma, welches von der Chromosphäre bis in die Korona reicht. Wegen der großen Temperaturunterschiede zwischen koronalem und Filamentplasma und aufgrund photosphärischer Absorption erscheinen Filamente auf der Sonnenoberfläche als dunkle Strukturen. Am Sonnenrand erscheinen Filamente in Emission als schleifenähnliche Gebilde, welche Protuberanzen genannt werden.

Um das Filament zu analysieren, nutze ich die Daten von zwei Instrumenten an Bord des Solar Dynamics Observatory (SDO), die Atmospheric Imaging Assembly (AIA) und den Helioseismic and Magnetic Imager (HMI). Ich nutzte fünf verschiedene extrem-ultraviolet (EUV) Wellenlängenbänder von AIA und die Kontinuumsbilder und Magnetogramme von HMI. Mit Hilfe der SolarSoft (SSW)-Bibliothek in der Programmiersprache Interactive Data Language (IDL) werden die Daten heruntergeladen und bearbeitet. Anschließend definiere ich einen ausgewählten Bereich (region-of-interest, ROI) der Größe 1088 Mm$\times$384 Mm um das Filament herum, bestimme eine Referenzzeit und korrigiere die differentielle Rotation für die gesamte Zeitreihe. Weiterhin nutze ich geometrische Korrekturen, um die Projektionseffekte zu beseitigen und bringe das Bild in ein äquidistantes Koordinatengitter.

Ich habe zwei verschiedene Datensätze: den Datensatz über eine lange Zeitdauer (long-duration data set) und den mit einer hohen zeitlichen Auflösung (high-cadence data set). Der erste enthält Bilder vom 8.–22. November 2011 mit einer Zeitauflösung von einer Stunde. Der zweite hat ein Zeitintervall von zwei Stunden am 16. November 2011 von 11:00 bis 13:00 UT, wenn das Filament durch den zentralen Sonnenmeridian läuft. Die Zeitauflösung beträgt dabei 12 s für die AIA Wellenlängenbänder 171 Å, 193 Å, 211 Å und 304 Å, 24 s für das AIA-Wellenlängenband 1600 Å und 45 s für die HMI Magnetogramme und Kontinuumsbilder.

Ich habe den ”long-duration” Datensatz genutzt um die zeitliche Entwicklung des Filaments zu untersuchen. Die unterschiedlichen Wellenlängen haben mir dabei geholfen, verschiedene atmosphärische Bereiche der Sonne zu sehen, von der Photosphäre über die Chromosphäre bis zur Korona. Zwei Eruptionen ereigneten sich während das Filament auf der Sonne sichtbar war. Das Filament verschwand mit der letzten Eruption als ein koronaler Massenauswurf. Außerdem habe ich die Chiralität des Filaments bestimmt. Das Filament ist dextral, was sehr typisch für die nördliche Hemisphäre ist. Die Chiralität gibt auch Informationen über die Helizität des Filaments. Zum Schluss erstelle ich ein Falschfarbenbild, bei dem drei verschiedene, temperatursensitive Spektrallinien aus unterschiedlichen Regionen der Korona genutzt werden. Die enthaltenden Farben sind an unser Farbempfinden angepasst.

Den ”high-cadence” Datensatz nutze ich, um die Dynamik des Filaments näher zu studieren. Dabei erstelle ich zunächst ein sensitives Magnetogramm, um die Feinstruktur des magnetischen Feldes stärker hervorzuheben. Weiterhin messe ich die magnetische Flusstransportgeschwindigkeit, welche ich mit der Geschwindigkeit von optischen Geschwindigkeitsfeldern in der Photosphäre, Chromosphäre und Korona vergleiche. Dafür benutze ich zwei unterschiedliche Algorithmen. Die magnetische Flusstransportgeschwindigkeit wird mit dem Differential Affine Velocity Estimator (DAVE) gemessen, welcher die räumlichen und zeitlichen Ableitungen im Magnetogramm nutzt, um die Geschwindigkeit zu bestimmen. Hierbei untersuche ich die Abhängigkeit der Geschwindigkeit vom Zeitintervall der Zeitreihe und vom Zeitintervall der zeitlichen Ableitungen. Um die Geschwindigkeit in der Photosphäre und Chromosphäre zu bestimmen, nutze ich Local Correlation Tracking (LCT), welches lokale Kreuzkorrelationen zwischen den aufeinander folgenden Bildern der Zeitreihe berechnet. Zum Schluss benutze ich eine neue Technik zur Bildverbesserung, die Noise Adaptive Fuzzy Equalization (NAFE) Methode, welche bei den AIA 171 Å-Bildern angewendet wird. Durch diese Methode ist es möglich, entgegenge-

setzt fließende Materiebewegungen entlang des Filamentrückens zu finden. Anschließend habe ich LCT verwendet, um Geschwindigkeiten in den EUV-Bildern zu bestimmen. Weiterhin wurde in einer kleinen Region die Abhängigkeit des Plasmageschwindigkeit vom Zeitintervall, über den die Geschwindigkeitskarte gemittelt werden, bestimmt. Um die entgegengesetzt fließenden Ströme zu bestimmen, wurde eine 32 Mm$\times$32 Mm große Region ausgewählt und eine Azimuth-Karte erstellt, bei der die Strömungsrichtung des Plasmas sichtbar gemacht wird. Sowohl mit dieser Karte als auch mit einer Karte für die Flussgeschwindigkeiten ist es möglich, diese Strömungen sowohl in dem 15-Minuten, als auch im 90-Minuten Zeitintervall nachzuweisen.

Chapter 1

Introduction

It became very dark for an hour or longer and the stars were visible and to men everything seemed as if it were green. The sun became like a crescent of the new moon and from its horns a glow like a roasting fire was coming forth and it was terrible for men to see the sign of the Lord. Then the sun cleared and we were happy again.

Chronicles of Novgorod, 1 May 1185 (Vyssotsky, 1949)

When the Moon covers the Sun completely and the Moon's shadow falls on Earth, it is called a total solar eclipse. This is a very rare event, which occurs on average every 400 years at the same place. By covering the bright solar disk, the outer atmospheric layers become visible, because they have much less intensity than the photosphere. The now appearing white light around the Sun is called corona, which means "crown" (Lang, 2001). In ancient times a total solar eclipse was a stressful and frightening experience. It was considered as a sign of the Lord or a precursor of the Apocalypse. The people were relieved, when the event passed by (see the description of the total solar eclipse on 1 May 1185, Vyssotsky, 1949). Later, it became possible to accurately calculate the occurrence of solar eclipses, for instance the one in 1860 in Spain. Many scientists observed this eclipse such as the astronomers A. Secchi and G. Tempel (see left panel in Fig. 1.1 of Eddy, 1974). However, even in our days a solar eclipse fascinates people and thus often is a medial event, e.g., the last total eclipse in Europe on 11 August 1999 (see right panel of Fig. 1.1). Many people observed this solar eclipse with special glasses protecting their eyes against the intense radiation from the Sun.

During a solar eclipse, it is possible to observe even more than the solar corona. Around the Sun loops become visible which appear like horns with *"a glow like a roasting fire"* (Vyssotsky, 1949). In Fig. 1.1 these loops are also notable. These loops are called prominences and reach from the photosphere up into the corona. Prominences observed on the solar disk are called filaments. Often both terms are used interchangeably in literature. Filaments are elongated and dense clouds of cool plasma suspended in the chromosphere and corona. They are best observed in the strong chromospheric absorption line Hα as dark structures.

1.1 Magnetic Field

The Sun's magnetic field is not static, it changes significantly during the eleven year solar cycle. An indication for the activity is the number of sunspots during the solar cycle. At solar minimum sunspots appear at high latitudes about $\pm 30^\circ$. There are also some sunspots of the old cycle remaining at about $\pm 10^\circ$. Three to four years after the beginning of cycle the sunspots appear as well at a maximum height of about $\pm 40^\circ$. With the progress of the cycle more sunspots appear on the solar surface at lower latitudes until they nearly reach the equator and the solar cycle repeats with sunspots appearing at high latitudes. The regions parallel to the equator, where the sunspots appear, are called activity belts.

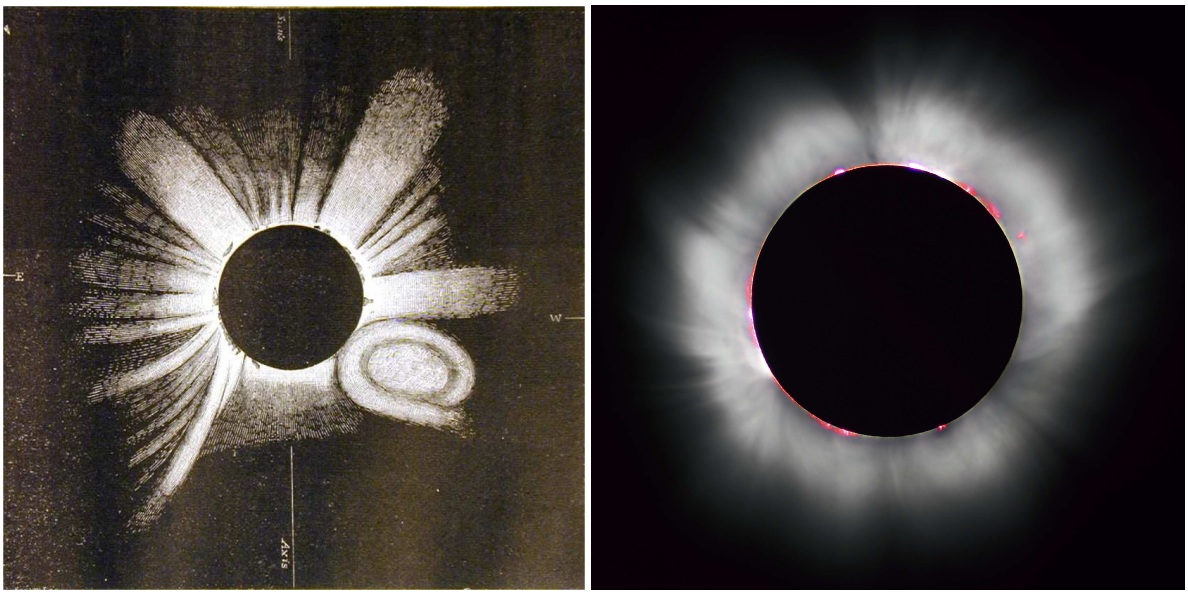

Figure 1.1: Left: Historical drawing of the corona during the solar eclipse on 18 July 1860 by G. Tempel at Torreblanca in Spain (see Fig. 2 in Eddy, 1974). This is probably the first recorded coronal mass ejection (CME) caused by a solar filament eruption. This eclipse appeared during the solar maximum. Prominences and other structures are also visible. Right: Image of the total solar eclipse on 11 August 1999 in Europe, France. The corona is visible with its bright glow as well as with some red glowing loops indicative of prominences around the solar disk.[1]

During most of the cycle coronal holes appear in polar regions (see Fig. 1.2). They are large regions of unipolar quiet-Sun magnetic fields and have very low emission in the (extreme) ultraviolet and X-ray regimes. In these regions, the magnetic field is open to the interplanetary space. They can reach widths from 40 to 300 Mm. Only during solar maximum they disappear. Coronal holes at lower latitudes are much less frequent (Schrijver and Zwaan, 2008).

At high latitudes ($> 45°$), filaments form between the activity belt and the polar regions. They can appear as a crown around the Sun and are thus appropriately called polar crown filaments. Typically, they appear at solar minimum (Cartledge, Titov, and Priest, 1996). The border between the activity belt and the coronal holes in the polar regions (Panesar *et al.*, 2014), where magnetic field lines of opposite polarities emerge in the photosphere, is called polarity-inversion line (PIL) or projected onto the local solar frame magnetic neutral line. Just above this PIL a filament channel can build up, and the filaments can evolve (Gaizauskas *et al.*, 1997). Filaments reach from the photosphere, where the footpoints of the filament are located, via the chromosphere into the corona. In the corona, the plasma can reach temperatures up to several million Kelvin (K), whereas the filament plasma has only temperatures of about 8000 K (Mackay *et al.*, 2010). There are two main reasons why filaments appear as dark structures in extreme ultraviolet (EUV) images, i.e., absorption and/or volume blocking. In the first case, the photospheric radiation is absorbed by hydrogen and helium resonance continua as it passes through the cool plasma of the filament. In the latter case, the big volume of cool plasma reduces the radiative output in comparison with the rest of the coronal plasma (Anzer and Heinzel, 2005; Panesar *et al.*, 2014).

Filaments are divided into three components: spine, barbs, and two extreme ends (Mackay *et al.*, 2010; Martin, 1998a). The spine, the biggest part of the filament, is a characteristic dark stretched-out structure. Barbs are like the legs of a filament, reaching from the corona down to the chromosphere, connecting to the footpoints of the filament rooted in the photosphere. The whole filament is a collection of small threads. Threads are thought to be aligned with the local magnetic field as a bundle of field lines. The plasma loops along the magnetic field lines crossing the PIL are called arcades. Above the photospheric PIL lies the filament channel in the chromosphere.

Polar crown filaments belong to the class of quiet-Sun filaments. Other kinds of filaments are intermediate filaments and active region filaments. The former are located at the outskirts of active regions and the latter inside active regions, e.g., in bipolar sunspot groups. Often a PIL and a filament channel are formed inside a decaying active region (Engvold, 1998).

[1] Photograph by Luc Viatour, *Solar Eclipse 1999*, accessed 29 January 2014, http://www.lucnix.be/v/Astronomy

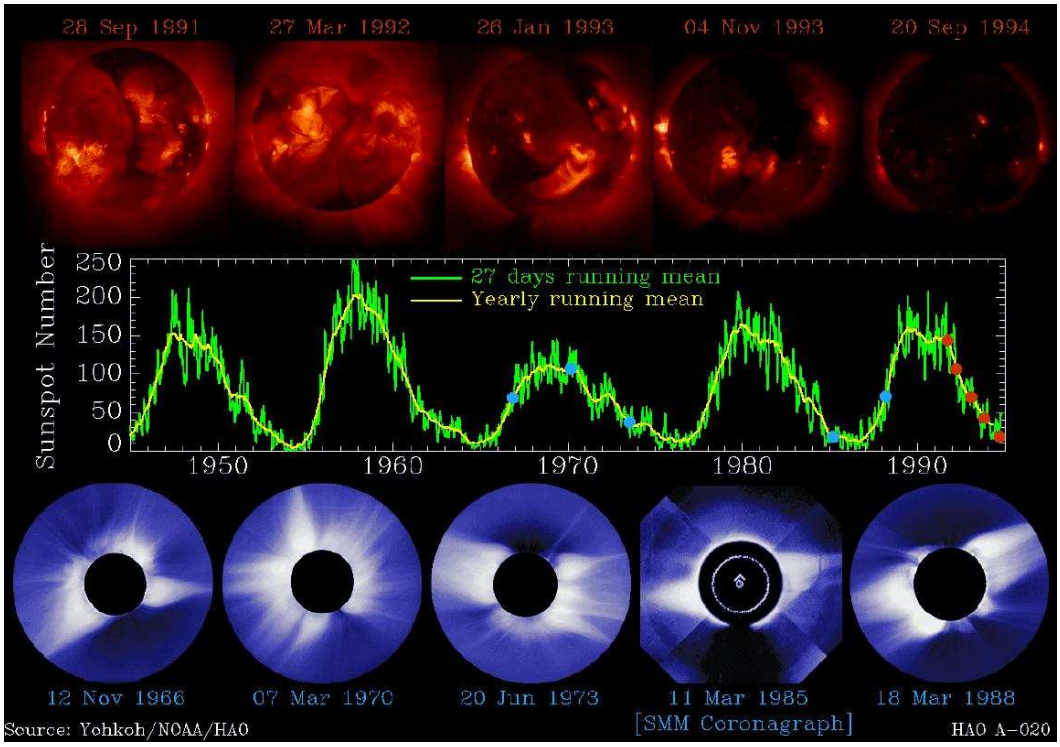

Figure 1.2: The middle row presents a diagram of the sunspot cycle from 1945 to 1995. The green line illustrates the mean number of sunspots over 27 days, and the yellow line denotes the yearly mean. The blue dots show when of the Solar Maximum Mission (SMM) coronagraph observed the image in the bottom row during the cycle from 1966 to 1988. The red dots portray X-ray (top row) images of the Sun from the maximum in 1990 to the minimum in 1994 acquired by the Yohkoh satellite. The reduced solar activity is clearly visible in the images. During most of the cycle coronal holes appear in the polar regions, but disappear during solar maximum.[2]

The appearance of quiet-Sun filaments is not bound to high latitudes but they can occur at any latitude. They can reach a height of 100 Mm above the photosphere and have a magnetic field of about 3–15 G (Leroy, Bommier, and Sahal-Brechot, 1983). The threads of quiet-Sun filaments are shorter than the threads of active region filaments (Mackay *et al.*, 2010).

The active region filaments appear in active regions around sunspots, i.e., only in the activity belt at latitudes of about $\pm 40°$. They only reach heights of around 10 Mm above the photosphere. This is just above the spicule forest, thus they are difficult to be observed above the solar limb. Spicules are thin, highly dynamic features in solar chromosphere. They transfer energy and mass from the photosphere to the corona (Pereira, De Pontieu, and Carlsson, 2012). The active region filaments can have a magnetic field strength of up to 600–700 G (Kuckein *et al.*, 2009) with relatively long threads. The different length of threads could be related to the angle of the magnetic field to the axis of the filament spine. The different filament types have also different lifetimes. Active-region filaments exist only for a few hours to days whereas quiet-Sun filaments are more stable structures and remain for several weeks. Intermediate filaments have values between those of active region and quiet-Sun filaments (Mackay *et al.*, 2010).

Filament plasma observed on the disk might not be the same as prominence plasma observed earlier or later above the limb, because of continuous changes in the fine structure of the prominence. Some filaments are clearly seen above the limb but not on the disk, because their temperatures (around 10^4 K) and densities are very low. They are no longer visible in Hα but in EUV (Mackay *et al.*, 2010).

The flow of the filament plasma gives us information about the role of the magnetic field. The flows can highlight the topology of the magnetic field (Alexander *et al.*, 2013). Zirker, Engvold, and Martin (1998) first described a bidirectional pattern of flows, which they called “counter-streaming”. Alexander *et al.* (2013) define these flows as “anti-parallel” flows, which describes better the opposite direction of the plasma stream along the filament threads. These flows are most clearly seen along the spine of the filament, but can also occur in the barbs (Zirker, Engvold, and Martin, 1998).

[2] P. Charbonneau and O. R. White, *The Sun: A Pictorial Introduction*, High Altitude Observatory, slides, 18 April 1995, accessed 30 January 2014, www.hao.ucar.edu/education/slides/slide20.php

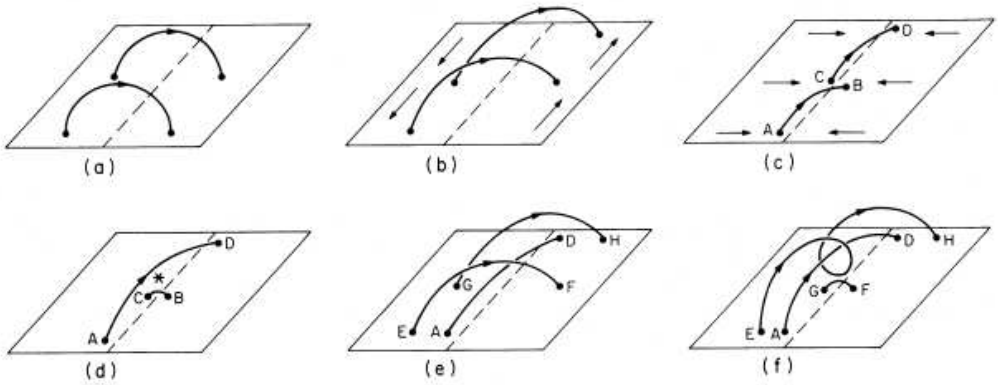

Figure 1.3: Formation of filaments according to the model of van Ballegooijen and Martens (1989). The rectangle shows the photosphere while the arcs reach up into the corona. The dashed line denotes the PIL. (a) The initial potential field. (b) Adding shear flows on both sides of the PIL stretches the magnetic field lines along the PIL. (c) By Adding converging flows, the magnetic field lines are pushed toward the neutral line. (d) Magnetic reconnection produces the shorter loop CB and the longer loop AD. (e) The loops EF and GH start with an initial potential field configuration (as seen in (a)), and then shear flows start again. (f) After reconnection the loops EH and GF appear. The loop GF submerges below the photosphere. The loop EH wraps around the loop AD and forms a spiral, which is called flux rope (see Fig. 1 in van Ballegooijen and Martens, 1989).

1.1.1 Formation of Filaments

After the formation of the filament channel the filament will develop. One model to explain the formation has been proposed by van Ballegooijen and Martens (1989). At time $t = 0$ the magnetic field lines are in a potential field configuration which connect the two different polarities. They form more or less perpendicular with respect to the PIL (Fig. 1.3a). By adding shear flows, the end points of the field lines are moved in opposite directions along the PIL (Fig. 1.3b). With a converging flow towards the PIL the end points of the field lines are approaching the neutral line and are very close to each other (Fig. 1.3c). Now, the field lines reconnect resulting in the smaller loop CB and the bigger loop AD (Fig. 1.3d). Magnetic buoyancy prevents the bigger loop AD from submerging below the photosphere, but the smaller loop CB might be pulled down below the photosphere. After a certain time the magnetic structure is pushed towards the PIL, and the process from (a) to (b) begins again (loops EF and GH in Fig. 1.3e). Because of reconnection, the loops GF and EH appear in Fig. 1.3f. The loop GF is pulled down, and the loop EF wraps around loop AD in form of a spiral, i.e., a flux rope (Fig. 1.3f). This process is repeated several times, and a helical structure is formed in the corona. The cool plasma of the filament is trapped inside the helical magnetic field lines. The source of the plasma is still unknown. One suggestion points to a siphon flow along the helical field lines transporting the plasma from the chromosphere up into the corona. Set off by the unstable magnetic field the prominence can erupt releasing plasma into space.

1.1.2 Chirality of Filaments

A certain handedness or chirality can be assigned to a filament (Zirker *et al.*, 1997). The smallest patterns on the Sun showing chirality properties are fibrils (Martin, 1998b). Filament channels can be identified by fibrils along the PIL and by the absence of short fibrils crossing the line (Zirker *et al.*, 1997). Viewing from the positive polarity side, the filament channel is dextral/sinistral if the fibrils stream out in the right/left direction. Dextral/sinistral filament channels are more frequently observed on the northern/southern hemisphere (see feature 1 in Fig. 1.4). The dextral or sinistral orientation of the filaments depends only on the hemisphere and not on the solar cycle. In addition, the barbs have a certain unambiguous orientation. Dextral filaments have always right-bearing barbs, and sinistral filaments have always left-bearing barbs (see feature 2 in Fig. 1.4). Furthermore, arcades show chirality patterns, too. For them the "skew" is defined as the acute angle between the loops and the filament axis (Martin, 1998b). The arcade is left-skewed if it is like a left-hand screw over the filament channel; and right-skewed like a right-hand screw. All left-skewed arcades straddle dextral filaments and all right-skewed arcades trace sinistral filaments (see feature 3 in Fig. 1.4). Both quiet-Sun and dynamic arcades have chirality re-

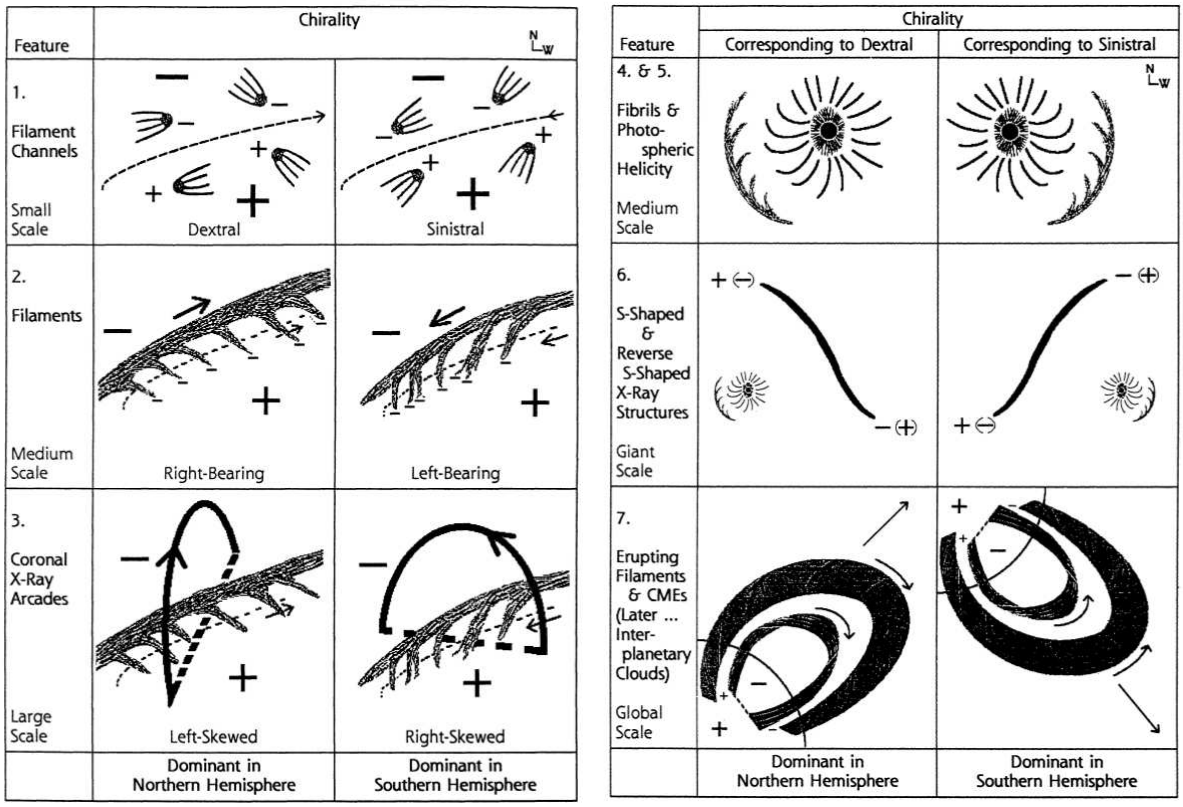

Figure 1.4: Chirality patterns of (1) fibrils and filament channels, (2) filaments and barbs, (3) coronal arcades, (4) and (5) fibrils and photospheric helicity, (6) large-scale X-ray structures, and (7) erupting filaments and CMEs. They are sorted by their dominant appearance on northern or southern solar hemisphere and by their one-to-one relationship. For example, the dextral fibrils and filament channels are dominant in the northern hemisphere and have always right-bearing barbs and left-skewed arcades (see Figs. 1 and 2 in Martin, 1998b).

lationships. Dynamic arcades can evolve after filament eruptions or coronal mass ejections (CMEs). The left-skewed arcades have then a rotation in the counterclockwise sense and right-skewed arcades in clockwise sense.

Zirker *et al.* (1997) give an explanation how the dextral and sinistral orientations of quiet-Sun filaments develop. They consider a bipolar magnetic region on the northern hemisphere at high latitudes with coronal loops nearly aligned in East-West direction. Due to differential rotation and supergranular diffusion the bipolar magnetic region is elongated and inclined to the equator. The coronal loops of the bipolar magnetic region are still nearly East-West oriented because of reconnection, and the short inner loops are pushed toward the PIL and into alignment with the PIL. Thus, the channel will be dextral.

Even bigger structures show chirality patterns such as superpenumbral fibrils around sunspots (Martin, 1998b). They have longer, conspicuous fibrils in active regions in an extended area beyond the penumbra of sunspots. The majority of fibrils in the northern/southern hemisphere have counterclockwise/clockwise patterns. To define the direction of the clockwise or counterclockwise patterns, one has to go along the fibrils from the outer to the inner end next to the penumbra (see features 4 and 5 in Fig. 1.4). The strongest curvature of fibrils is visible near filaments or filament channels. Active regions in general show chirality features. In the northern/southern hemisphere the active regions are dominantly negative/positive. However, the whole active region has not necessarily the same chirality. It has only a dominant sense of chirality.

Furthermore, Martin (1998b) describes the chirality of erupting filaments (see feature 7 in Fig. 1.4). The helical magnetic field lines of the filament rise and form CMEs. They have in most cases the same chirality as the arcades of the filament. Left-skewed arcades of dextral filaments evolve to left-helical CMEs. The ejected part of a CME is called an interplanetary cloud. Left-helical CMEs will form left-helical interplanetary clouds. The same reasoning applies to right-skewed arcades forming right-helical CMEs. But also dextral filaments forming right-helical twist or vice versa were observed. In the pre-eruptive or early eruptive stage the chirality of the CME is decided via reconnection.

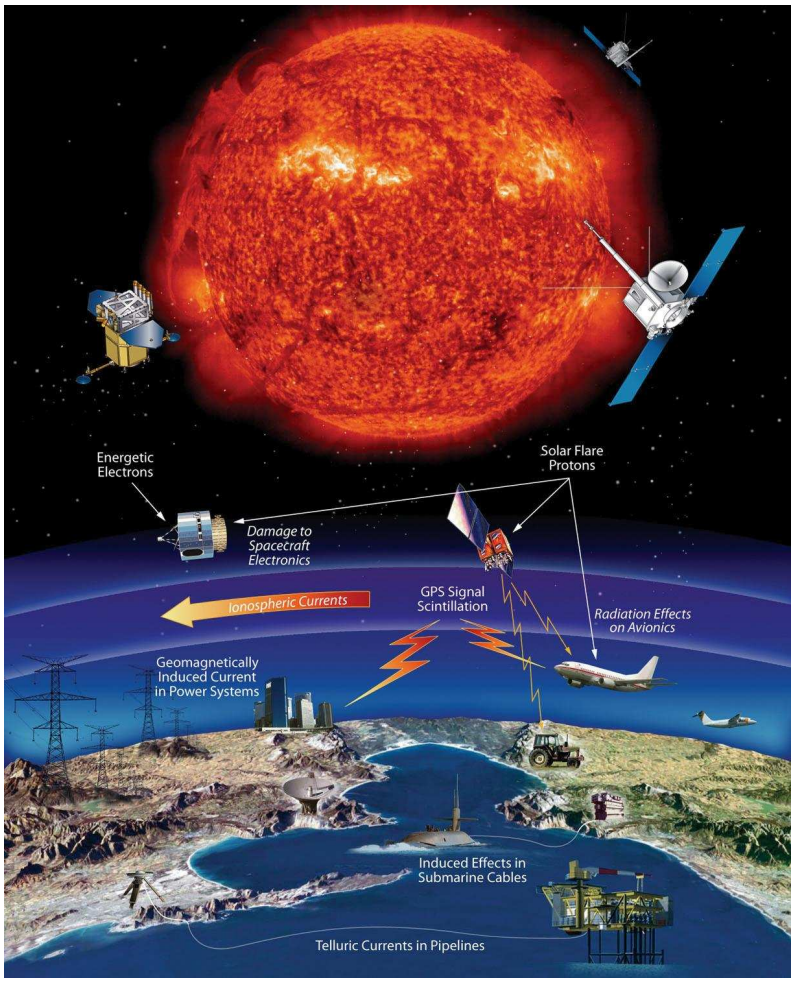

Figure 1.5: Space-weather effects on Earth and in near-Earth environment are caused by the solar wind, flares, and CMEs. High-energy particles from solar flares or CMEs can damage spacecraft electronics and destroy solar cells. Flares can also disturb GPS signals, which are used to navigate cars or airplanes, and have radiation effects on avionics. Furthermore, space-weather effects can cause geomagnetically induced currents, which damage submarine cables, power grids, and cause corrosion in pipelines.[3]

1.2 Space Weather

Space weather summarizes effects on the Earth's atmosphere and the near-Earth environment, which are caused by high-energy particles and electromagnetic radiation from the Sun. Their sources are the solar wind, CMEs, or solar flares. The solar wind is a constantly changing stream of charged atoms and sub-atomic particles. When it reaches the Earth's atmosphere it causes aurorae, the northern and southern lights, which are very beautiful events. However, high-energy particles can also cause large electric currents, which interrupt communication systems and adversely affect satellite navigation and power grids (see Fig. 1.5). A more powerful event is a solar flare. Thereby an enormous amount of energy is released in few minutes with temperatures up to 100 million Kelvin. Additionally, it causes signal scintillation and disturbs reception of radio signals. When a filament erupts, a large cloud of solar atmospheric plasma is ejected into space. Big eruptions like this are called CMEs. Some but not all flares can cause CMEs. Pointing towards Earth, they can disturb technical systems such as radio communication and satellite navigation; but also increase radiation exposure for astronauts, airline crews and passengers as well as disrupt power systems and even cause pipeline corrosion. In our technological society such solar events are potentially dangerous (Moldwin, 2008).

The goal of solar physics is to improve our understanding of the dynamics of the Sun to forecast events such as CMEs and solar flares. For this reason, we are interested in the origin of such space-weather events. In the next chapters the dynamics and evolution of a giant solar filament will be analyzed. This filament had two eruptive phases: the first when it rotated on the solar surface and the second at the end of its lifetime. Both eruptions were not pointing towards Earth, thus no major effects were observed on Earth. This filament is also special because of its enormous length. Only a few examples of such giant quiet-Sun filaments have been observed and reported in literature.

[3] Jennifer Rumburg, *Solar Storm and Space Weather – Frequently Asked Questions*, last updated: 30 September 2013, accessed 6 January 2014, www.nasa.gov

Chapter 2

Solar Dynamics Observatory

In a new adventure of discovery no one can foretell what will be found, and it is probably safe to predict that the most important new discovery that will be made with flying telescopes will be quite unexpected and unforeseen.

Spitzer (1961)

The Solar Dynamics Observatory (SDO) is the successor of the Solar and Heliospheric Observatory (SoHO, Domingo, Fleck, and Poland, 1995) mission, which was launched in 1995. The SDO spacecraft lifted off from the Kennedy Space Center (KSC) almost 15-years later on 11 February 2010 to investigate the Sun's magnetic field on a nominal five-year mission (Pesnell, Thompson, and Chamberlin, 2012). As part of the Living with a Star (LWS) program, SDO investigates the influence of the variable Sun on life on Earth and technological systems; and the role of solar variation in the change of Earth's atmosphere and climate. Every LWS mission has been designed to answer another specific science question. In particular, SDO shall determine the origin, the generation and the structure of the magnetic field, as well as the formation of active regions, thus improving our understanding of the solar cycle and aiding in the prediction of space-weather events. With respect to space weather, SDO addresses the questions how the stored magnetic energy is released and how it influences our daily life. Together with other space missions, such as SoHO and Hinode (Kosugi *et al.*, 2007), a whole magnetic cycle of 22-years can be observed and analyzed. With the help of SDO data, the prediction of solar activity, flares or CMEs, becomes possible, and even solar activity in future cycles can be anticipated. In any case, SDO data will help scientists to understand the physics of solar variation and how it influences our daily life and society (Pesnell, Thompson, and Chamberlin, 2012).

In one day SDO sends 1.5 terabytes of raw data to Earth; in total collecting about 3–4 petabytes of data during the primary mission lifetime. The data contain 150.000 high-resolution full-disk images of the Sun and 9000 EUV spectra each day. To send the data, SDO has a 6-meter-long high-gain antenna (see Fig. 2.1). The total mass of SDO is 3000 kg: the spacecraft has a weight of 1300 kg, the instruments bring together 300 kg, and the rest is fuel. Along the sun-pointing axis the spacecraft has a length of 4.7 m and each side has a length of 2.2 m. The solar panels have a collecting area of 6.6 m^2 and deliver 1500 W of energy (Pesnell, Thompson, and Chamberlin, 2012).

Three instruments are on board SDO: the Atmospheric Imaging Assembly (AIA), the Extreme ultraviolet Variability Experiment (EVE), and the Helioseismic and Magnetic Imager (HMI). In this thesis, we use AIA and HMI data. The instruments EVE and AIA focus on the analysis of EUV radiation from 1–122 nm, which cools the solar corona and is the dominant source for heating Earth's atmosphere (Pesnell, Thompson, and Chamberlin, 2012). The goal of EVE (Woods *et al.*, 2012) is to observe the most variable and unpredictable part of solar spectrum, i.e., the EUV from 0.1–105 nm and 121.6 nm to get real-time space-weather products and to further our knowledge of the rapidly evolving solar flares.

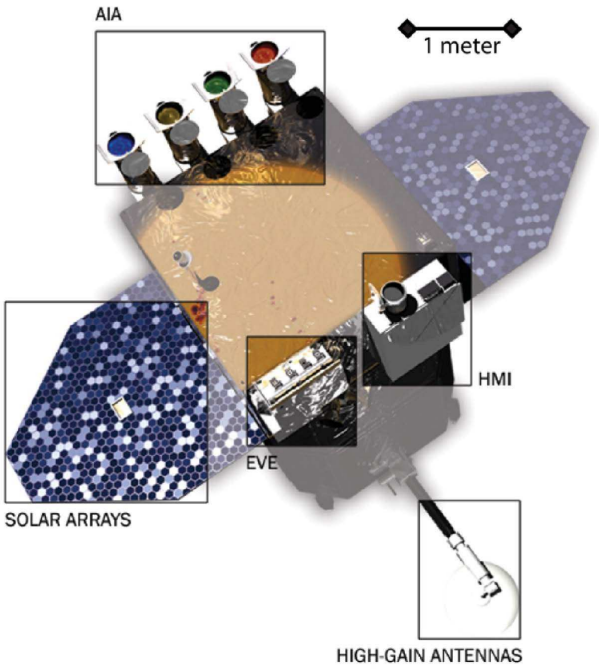

Figure 2.1: The Solar Dynamics Observatory (SDO) with its main instruments: Atmospheric Imaging Assembly (AIA), Extreme ultraviolet Variability Experiment (EVE), and Helioseismic and Magnetic Imager (HMI). The deployed high-gain antenna has a length of 6 m and the solar panels have a collecting area of 6.6 m^2 (see Fig. 1 in Pesnell, Thompson, and Chamberlin, 2012).

Table 2.1: The different channels in which AIA observes. Seven band passes are centered on EUV emission lines, one is centered on UV, and three are dedicated to continuum measurements (adapted from Tab. 1 in Lemen *et al.*, 2012).

Channel	Primary ions	Atmospheric region
4500 Å	continuum	photosphere
1700 Å	continuum	temperature minimum and photosphere
304 Å	He II	chromosphere and transition region
1600 Å	C IV and continuum	transition region and upper photosphere
171 Å	Fe IX	quiet corona and upper transition region
193 Å	Fe XII and Fe XXIV	corona and hot flare plasma
211 Å	Fe XIV	active-region corona
335 Å	Fe XVI	active-region corona
94 Å	Fe XVIII	flaring corona
131 Å	Fe VIII and Fe XXI	transition region and flaring corona

2.1 Atmospheric Imaging Assembly

Four telescopes comprise AIA (see Fig. 2.2). They observe the solar surface and atmosphere focusing on the evolution of the magnetic environment. In the corona the magnetic field evolves on time scales ranging from seconds to years (Lemen *et al.*, 2012). Full-disk images of the atmosphere taken with AIA have a field-of-view (FOV) of $41' \times 41'$, an image scale of $0\farcs6$ $pixel^{-1}$, and a spatial resolution of $1\farcs5$. The four Cassegrain telescopes have in total 10 different wavelength bands. Each 20-centimeter telescope has a filter wheel to select between a shorter or longer band pass. Telescope number one contains filters centered at 131 Å and 335 Å, telescope number two centered at 194 Å and 211 Å, and telescope number four centered at 94 Å and 304 Å; all band passes are situated in EUV. Only telescope three has four filters; on one half is the filter for EUV, which is centered at 171 Å, and on the other half the filter is split into three band passes centered at 1600 Å, 1700 Å, and 4500 Å, which observe in ultraviolet (UV) and continuum. With the different filters, it is possible to observe different parts of the solar atmosphere. Table 2.1 presents a complete overview of the observed atmospheric layers.

The CCD cameras take high-resolution (4096×4096 pixels) full-disk images of the Sun. With the six EUV channels, which observe the emission of ionized iron, it is possible to construct relatively narrow-band temperature maps of the solar corona from $1–20 \times 10^6$ K (Lemen *et al.*, 2012).

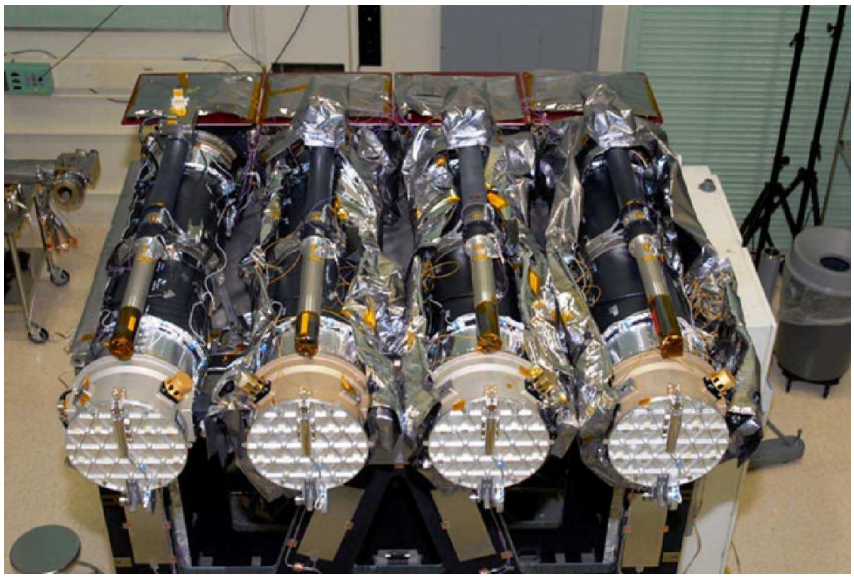

Figure 2.2: The instrument package of AIA consists of four telescopes, each of which has its own guiding telescope mounted on top. The instrument has been assembled in a clean room at NASA Goddard Space Flight Center before being mounted on the SDO spacecraft (see Fig. 1 in Lemen *et al.*, 2012).

In detail, AIA will research the dynamics of coronal structure, how energy is brought into the coronal field, and how it is stored and released (Lemen *et al.*, 2012). In addition, the geometry of the magnetic field will be analyzed. The high-energy radiation effects the ionization of Earth's upper atmosphere and can thus disturb communication systems on Earth, damage spacecraft electronics, and deteriorate solar panels in low-Earth orbit. The sources of space-weather events are CMEs and solar flares. The instrument is designed to collect information to understand the sources of radiation and high-energy particles and to predict them. A new field of observation is coronal seismology, which studies oscillations and waves and retrieves fundamental physical properties such as the magnetic field, temperature, and viscosity.

2.2 Helioseismic and Magnetic Imager

The Helioseismic and Magnetic Imager (HMI, Schou *et al.*, 2012) measures the Dopplershift, the intensity, the vector magnetic field, and the line-of-sight (LOS) magnetic field in the solar photosphere using the Fe I λ6173 Å line. The filtergrams are observed at six positions in the range $\pm$172.5 mÅ around the line core of the Fe I λ6173 Å line. The two HMI CCD cameras have a resolution of 4096$\times$4096 pixels, an image scale of $0\farcs5$ pixel^{-1}, and a spatial resolution of $0\farcs9$. The filtergraph takes a series of images at different wavelength positions and polarization states and combines them to derive the physical parameters. The camera takes a full-disk image every 3.75 s giving an overall cadence of 45 s for Dopplergram, intensity, and LOS magnetic field measurements. The full vector magnetic field map (vector-magnetogram) has a slower cadence of 90 to 135 s. The design is based on the Michelson Doppler Imager (MDI, Scherrer *et al.*, 1995) on board of SoHO but with improvements, e.g., it has the capability to observe the full Stokes profiles.

Linking the internal processes and the dynamics of the corona and heliosphere becomes possible with the help of filtergrams. The instrument studies convection-zone dynamics, the solar dynamo, and the origin and evolution of sunspots and active regions. Furthermore, HMI will research the sources of solar magnetic activity and is used to predict space weather. As the name implies HMI has been designed for helioseismology, which is used to take a glimpse at the Sun's interior, just like seismology on Earth. Helioseismology uses solar oscillations to probe flows and structures in the interior regions of the Sun (Scherrer *et al.*, 2012). The full-disk filtergram data of HMI are downlinked without any processing other than hardware compression and encoding. The data processing is then carried out on ground (Scherrer *et al.*, 2012).

2.3 Data Handling and Processing

The data are transmitted to two SDO ground stations in New Mexico. Afterward AIA and HMI data are transferred to the Joint SDO Operations Center (JSOC) Science-Data Processing (SDP) facility at

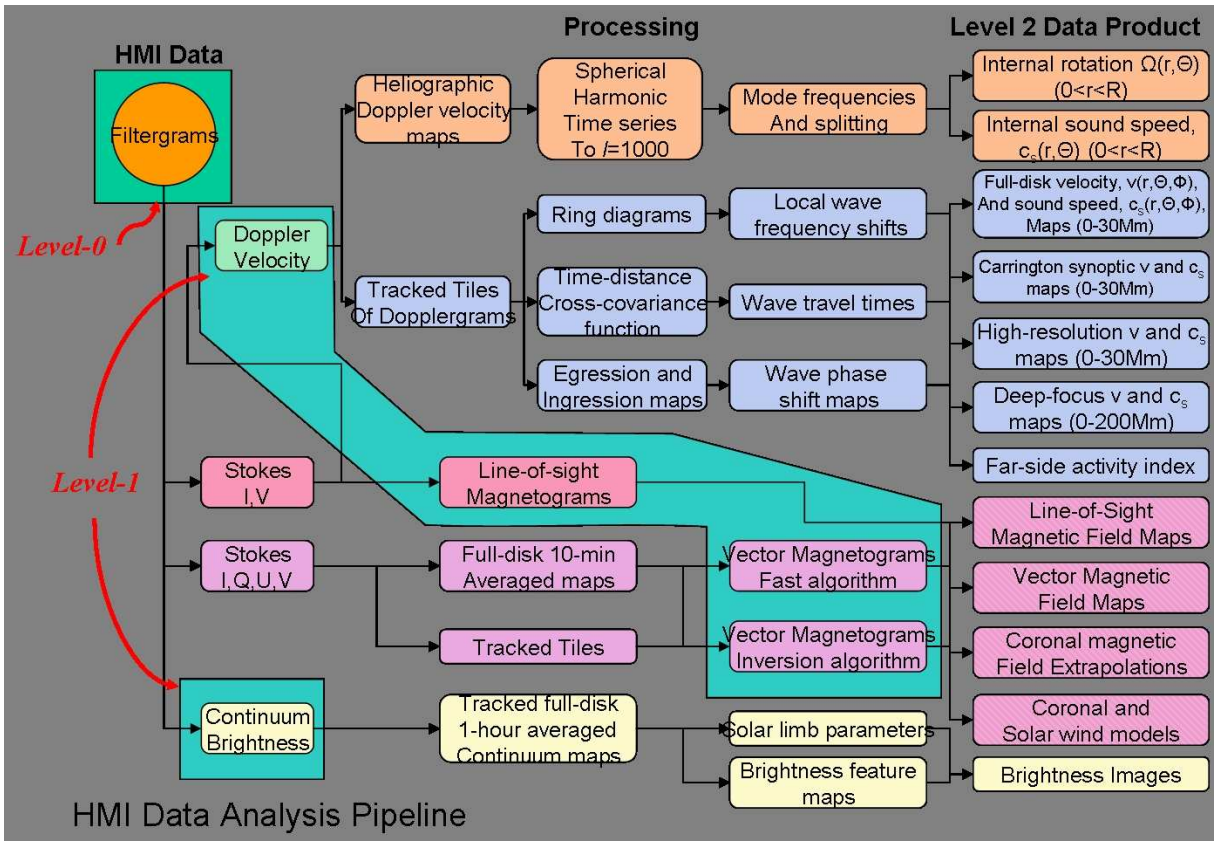

Figure 2.3: Data processing steps of HMI data. The filtergrams arrive at the ground station and will be used to create the continuum images. The Stokes vector data are used to produce the Doppler velocity maps and the magnetograms. The Dopplergrams are the main input for helioseismology, which is the primary science objective of HMI. We use in our study information about the LOS magnetic field to get information about dynamics of the magnetic features.[1]

Stanford University. At the ground station the data are stored 30 days to mitigate the risk of data loss, in case of problems with the network or at JSOC-SDP. At Stanford University the data arrive only minutes after they have been acquired in orbit. The non-processed data, i.e., Level 0 data, will be archived there (Lemen *et al.*, 2012), and duplicates are stored on 800 Gbytes tapes at the instrument operation center, the Lockheed Martin Solar and Astrophysics Laboratory's (LMSAL).

2.3.1 Processing of AIA Data

The AIA data are stored in the data archive of JSOC-SDP as 16-bit integer 4096×4096 pixels images. On the spacecraft the data are Rice compressed (Rice and Plaunt, 1971) to reduce the ground storage requirements. Now the so-called Level 0 data have to go through several processing steps (Lemen *et al.*, 2012). First the dark images are subtracted, and a flat-field correction is carried out. A further step is to correct "bad" pixels, which do not respond correctly to light. They are replaced by values of the neighboring pixels. Typically, only a small number (0.1%) is affected. Whenever high-energy particles hit the CCD camera or interact with the instrument, they are leading to "spikes" in the images. To remove them, an algorithm is used, which compares each pixel with its neighboring pixels. When a pixel value is not statistically consistent, it will be replaced by the average value. The Sun's rotation axis, like Earth's axis, is tilted with respect to the ecliptic. Therefore, the images are rotated such that North is on the top, and East is on the left of the image. The thus created Level 1.0 data are exported as Flexible Image Transport System (FITS, Hanisch *et al.*, 2001; Wells, Greisen, and Harten, 1981) files represented as 32-bit floating values.

[1] Helioseismic and Magnetic Imager – Stanford Solar Group, *Data Analysis Pipeline*, accessed 18 December 2013, hmi.stanford.edu

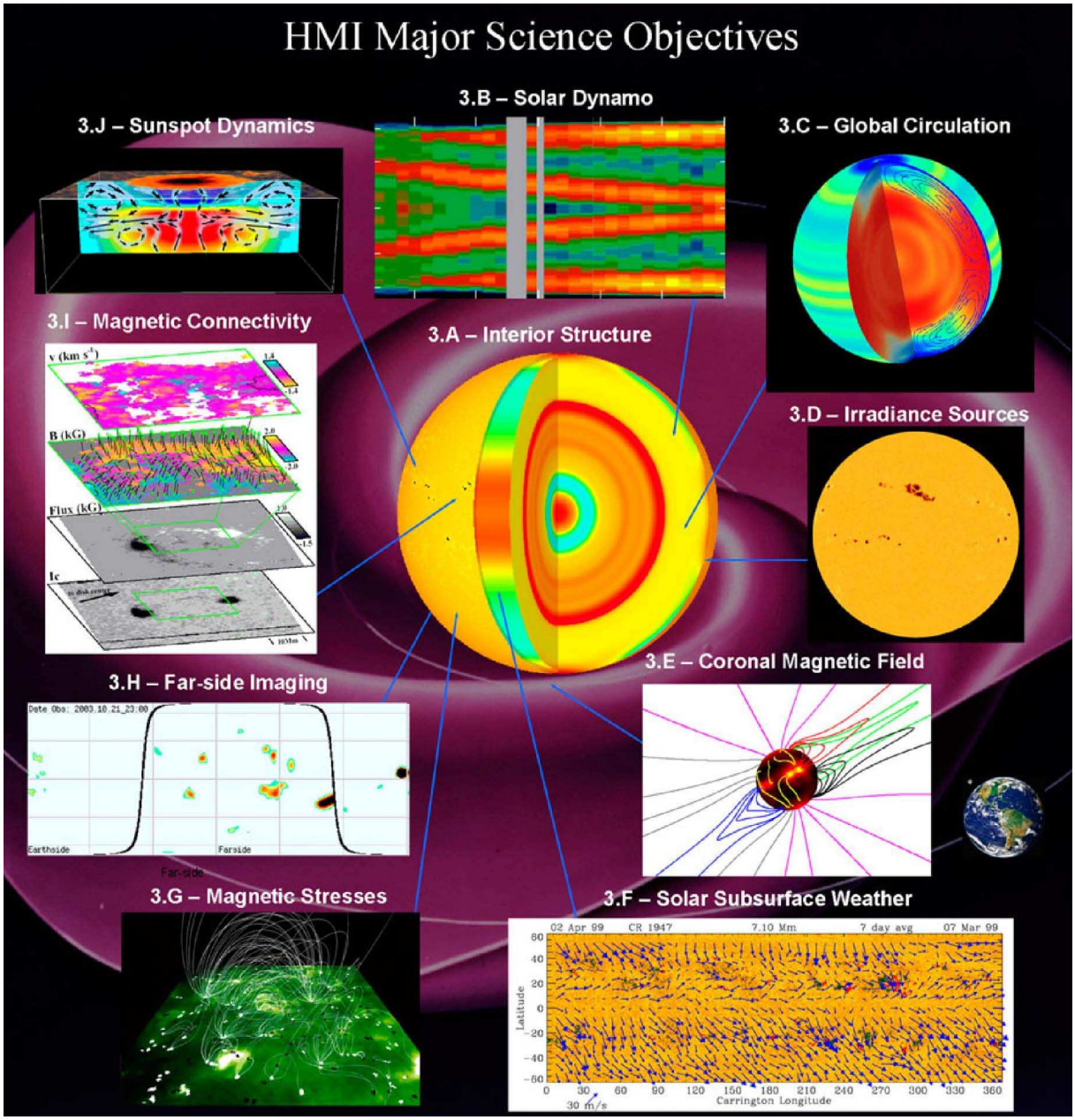

Figure 2.4: The main science objective of HMI (see Fig. 3 in Scherrer *et al.*, 2012) is helioseismology, i.e, the (A) interior structure of the Sun will be analyzed. This yields additional information about (B) the solar dynamo and (C) the global circulation. Helioseismology also enables (H) far-side imaging. In this thesis we concentrate on (I) the magnetic connectivity in the quiet Sun and analyze the dynamics of a solar filament similar to task (J) for sunspots. Yet even more can be done with HMI data, i.e, the analysis of the higher layers of the Sun: (D) studying the variation of the solar irradiance, (E) characterizing the coronal magnetic field, and (G) determining how magnetic stresses of these fields lead to solar eruptive events.

2.3.2 Processing of HMI Data

The Level 0 raw data from the telemetry stream are filtergrams (DeRosa and Slater, 2013). These filtergrams are converted to Level 1.0 data by using similar processing steps as for AIA data. First the bad pixels are removed, then the flat-fielding and the quality assessment checks are performed. All these processing steps are reversible. The next step is to construct the physical observables (Dopplergrams, continuum images, and LOS and vector magnetograms) from the filtergrams (see Fig 2.3). The photospheric continuum images are taken near the Fe I λ6173 Å absorption line. To create the Dopplergrams and the LOS magnetograms, the two Stokes profiles I and V are used; to construct the vector magnetograms, all four Stokes profiles are used (see Fig 2.3). Level 2 data is produced with further processing. These data are irrevocably filtered, time-sequence-merged or Fourier transformed. The Dopplergrams facilitate global and local helioseismology; based on their time-series, the mean rotation and sound speed

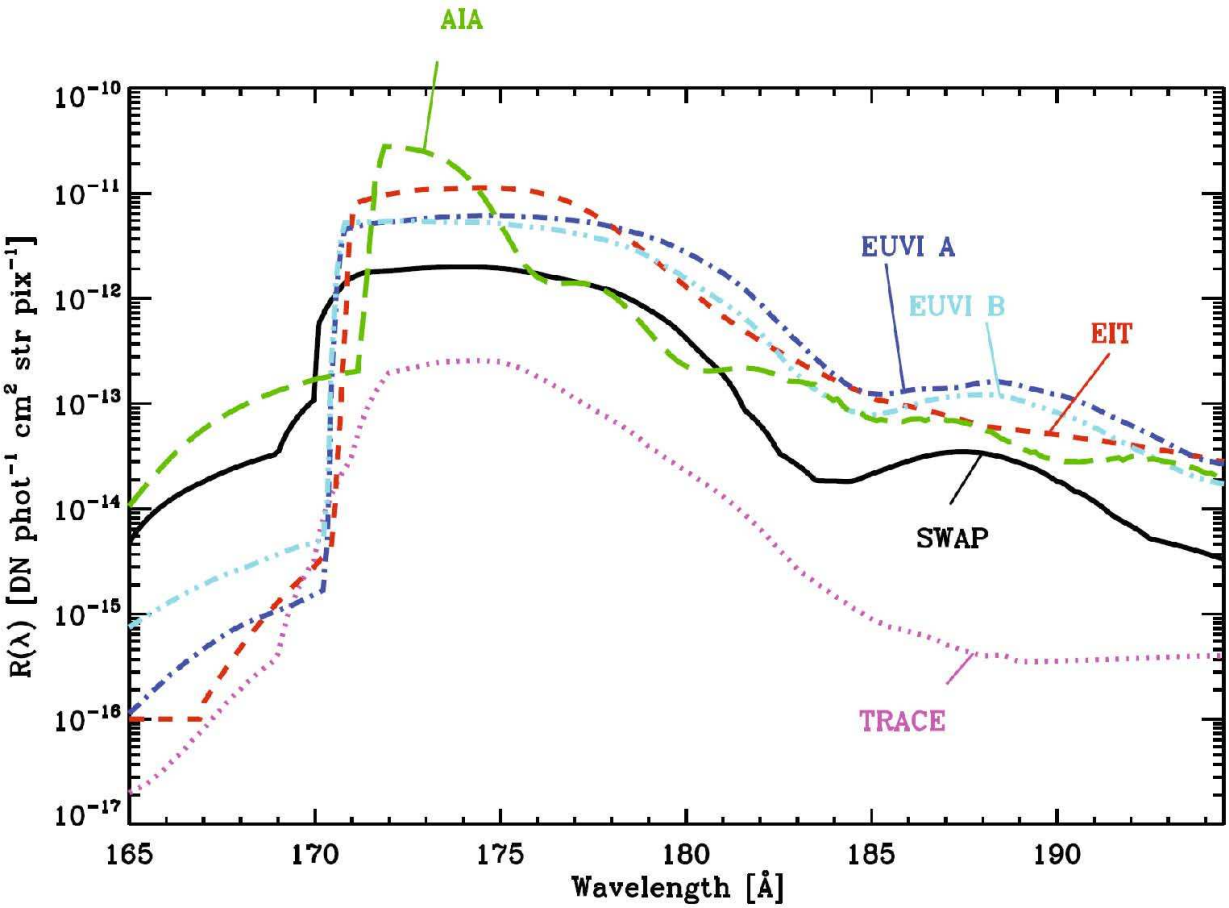

Figure 2.5: Comparison of the wavelength response functions $R(\lambda)$ of different EUV imagers at wavelength 171 Å: AIA (green), TRACE (pink), SWAP (black), EIT (red), and EUVI S1 filters (light and dark blue). The shapes of each wavelength response function are different. The AIA response function has the highest peak. The other have a more extended plateau around the peak wavelength of 171 Å (see Fig. 2 in Raftery *et al.*, 2013).

in the Sun's interior can be derived. Dopplergrams are also used to sense the presence of active regions before they rotate on the Earth-facing hemisphere, or before they have fully emerged on the surface. The magnetic data products are used to create synoptic maps, detect locations of surface activity, or create coronal and solar wind models for space-weather forecast. The Level 2 data products and major science objectives of the HMI are shown in Fig. 2.4: (A) sound-speed variation relative to the standard solar modal, (B) solar-cycle variation, (C) solar meridional circulation and differential rotation, or (I) the vector field image showing the magnetic connectivity in sunspots (Scherrer *et al.*, 2012).

To directly compare AIA and HMI data, HMI data have to be rescaled down to $0\farcs6$ pixel^{-1}, so that both data sets have the same spatial resolution. The processed AIA and HMI data are available to the public 48 h after they were received by JSOC.

2.4 Wavelength and Temperature Response Function

The wavelength response function $R(\lambda)$ shows the sensitivity of an imager to emission at different wavelengths (Raftery *et al.*, 2013). It can be calculated from the instruments' parameters by combining measurements of the entrance filter, effective area, and CCD quantum efficiency (Boerner *et al.*, 2012)

$$R(\lambda) = A_{\text{eff}}(\lambda) \cdot G(\lambda). \tag{2.1}$$

Therefore, the gain G of the CCD is measured in data numbers (DN) phot^{-1}, and the effective area A_{eff} is given in centimeters squared. The latter contains information about the efficiency of the telescope optics. Each component can be calculated or measured separately to obtain the overall wavelength response function.

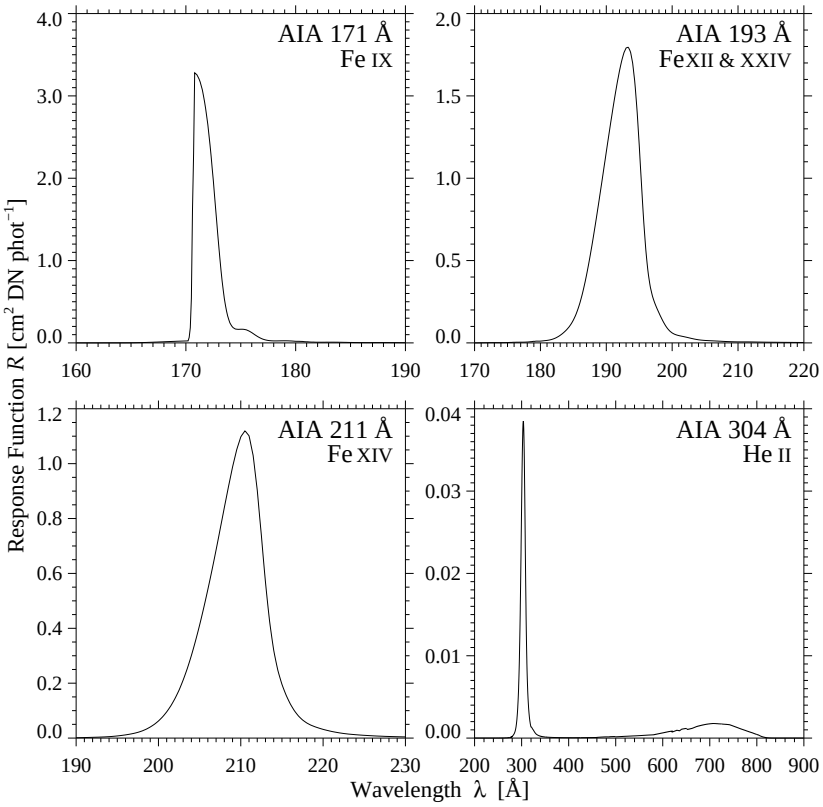

Figure 2.6: Wavelength response function for AIA images with wavelength 171 Å, 193 Å, 211 Å, and 304 Å. The maximum is reached at the wavelengths 170.8 Å, 193.3 Å, 210.5 Å, and 304 Å. The values of the response function maximum are between 1 cm^2 DN $phot^{-1}$ and 4 cm^2 DN $phot^{-1}$ except for the 304 Å line. There the response function reaches only values of around 0.04 cm^2 DN $phot^{-1}$. This line is a helium line and the other lines are iron lines.

Raftery *et al.* (2013) compare the response function of the 171 Å pass-bands for six instruments: Sun Watcher with Active Pixels and Image Processing (SWAP, Berghmans *et al.*, 2006) on board the PRoject for OnBoard Autonomy 2 (PROBA2, Santandrea *et al.*, 2013) satellite, Extreme Ultraviolet Imaging Telescope (EIT, Delaboudinière *et al.*, 1995) on board of SoHO, Transition Region and Coronal Explorer (TRACE, Handy *et al.*, 1999) , Extreme Ultraviolet Imagers (EUVI, Howard *et al.*, 2008) on board the Solar TErrestrial RElations Observatory (STEREO, Kaiser *et al.*, 2008) A and B spacecrafts, and AIA on board SDO. Some response functions are determined experimentally using full end-to-end throughput tests (e.g., SWAP). Figure 2.5, taken from Raftery *et al.* (2013), shows a comparison of the 171 Å response functions for the six different instruments. Apparently, the AIA response function has the highest peak response, and the overall shape of its response function differs from the shape of all the others. The AIA $R(\lambda)$ has its maximum at $2.7\times\ 10^{-11}$ DN $phot^{-1}$ cm^2 str $pixel^{-1}$ and a maximum response at 171.8 Å with a plateau width of around 2 Å. Furthermore, the AIA response function shows four successive humps at 177.5Å, 182Å, 187Å, and 192.5 Å. The TRACE response function has a similar shape as the AIA response but with a reduced maximum. The other four response functions of SWAP, EUVI-A, EUVI-B, and EIT have a very sharp rise between 170 and 171 Å, reaching values between 1.6–$7.9\times\ 10^{-12}$ DN $phot^{-1}$ cm^2 str $pixel^{-1}$ at around 171 Å. Having reached their respective maxima, all four response functions level out and have a plateau with a width of 6 ± 2 Å.

The high-cadence, high-resolution AIA images are taken in ten pass-bands (EUV, UV, and optical), which is more than any other instrument accomplished before. The AIA telescopes select between the different wavelength bands using broad band filters. Each filter has its own response function centered on the observed spectral line. The response function can be accessed through SolarSoft (SSW, Freeland and Handy, 1998; Bentely and Freeland, 1998), a software library written in IDL.[2] In principle it is possible to display the AIA response function for all ten wavelengths. However, in Fig. 2.6 only four wavelengths (171 Å, 193 Å, 211 Å, and 304 Å) are shown because they are used later in the analysis. The maxima of the different wavelength responses are near the center of the spectral lines; the maximum of the wavelength response for the 171 Å line is at 170.8 Å, for the 193 Å line at 193.3 Å, for the 211 Å line at 210.5 Å, and 303.5 Å for the 304 Å line. The maximum for the 171 Å line is at a lower wavelength (171.8 Å) than shown in the results of Raftery *et al.* (2013).

[2] www.exelisvis.com

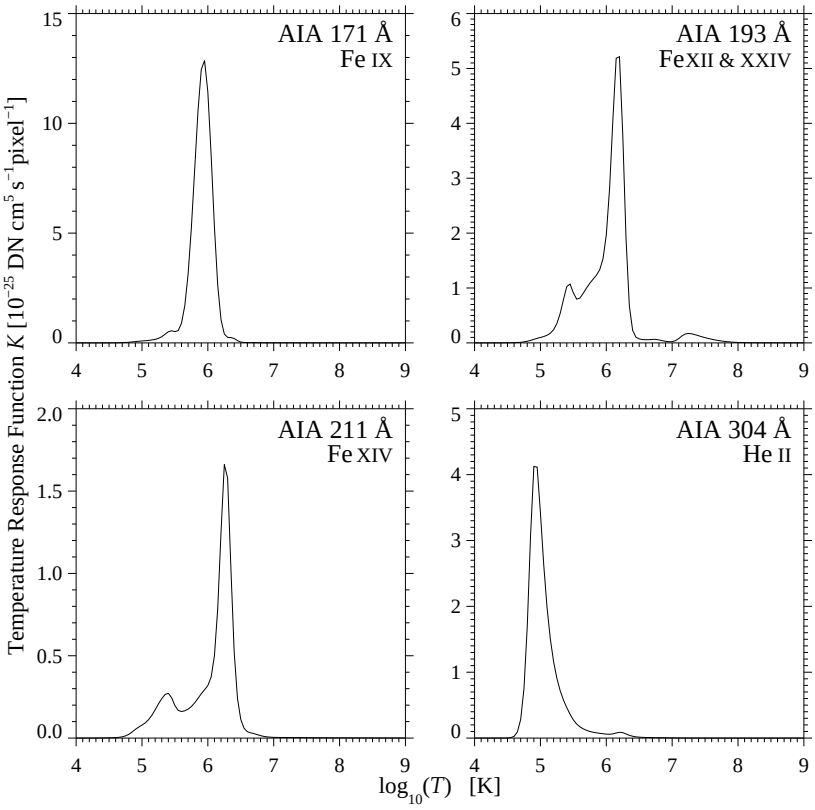

Figure 2.7: Temperature response function $K(T)$ for AIA images. The maximum values of the response function are at the temperatures 0.89 MK for 171 Å, at 1.58 MK for 193 Å, at 1.78 MK for 211 Å, and at 0.79 MK for 304 Å. The response function K reaches values between 1.7 and 13 DN cm^5 s^{-1} pixel^{-1} at the maximum.

Raftery *et al.* (2013) explains that the temperature response function $K(T)$ is calculated by multiplying the wavelength response function $R(\lambda)$ with a solar spectrum generated at that temperature. To calculate the typical spectral contribution function $G(\lambda, T)$ the CHIANTI atomic-physics package (Dere *et al.*, 1997) was employed. It uses a constant emission measure value of 10^{20} cm^{-5} and isothermal temperature values between 0.5 and 20 million Kelvin (MK) in steps of $\delta \log(T) = 0.1$. The intensity of an emission line depends on the population of the upper level of the atomic transition, which itself depends on the plasma density. Here a standard coronal density of 5×10^9 cm^{-3} is assumed. The CHIANTI function $G(\lambda, T)$ and the wavelength function $R(\lambda)$ are convolved to calculate the temperature response function

$$K_i(T) = \int_0^\infty G(\lambda, T) \cdot R_i(\lambda)\, d\lambda. \tag{2.2}$$

The different channels of AIA are represented by the index i. CHIANTI does not model the He II λ304 Å line very well and thus needs an empirical correction factor of 20 (Boerner *et al.*, 2012).

The temperature response functions for the different EUV wavelengths of AIA are displayed with help of SSW routines (see Fig. 2.7). The values for the temperature are given on a logarithmic scale; the temperature response function $K(T)$ is given in 10^{-25} DN cm^5 s^{-1} pixel^{-1}. The maximum values of the temperature for each wavelength differ: for 171 Å the maximum is 0.89 MK, for 193 Å it is 1.58 MK, for 211 Å it is 1.78 MK, and for 304 Å it is 0.79 MK. The spectral lines originate in different layers of the corona and chromosphere (Tab. 2.1). The spectral line at 304 Å covers the chromosphere which has much lower temperatures than the corona. The other spectral lines have their origin in the corona.

2.5 General Description of the Filament

Long quiet-Sun filaments at high latitudes (>45°) are called polar-crown filaments because they lie around the pole roughly along the same line of latitude (parallel to the equator) forming a crown. The observed filament is a quiet-Sun filament which does not fit into the category of a polar-crown filament. This giant filament is interesting to study because in literature only a few giant quiet-Sun filaments are

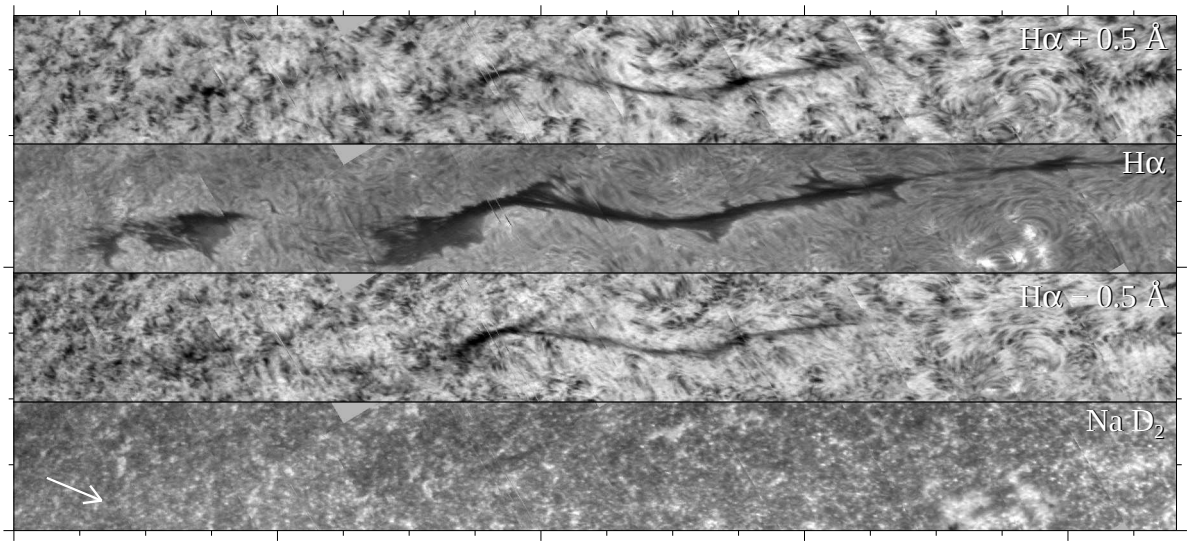

Figure 2.8: The filament observed in Hα on 15 November 2011 (2$^{\text{nd}}$ row). Above and below are images of H$\alpha + 0.5$ Å and H$\alpha - 0.5$ Å, and a Na D_2 line core image in the bottom row. The Hα line center image shows that the filament has a gap on its left side because of an eruption a few hours before. In addition, an emerging flux region is visible as bright spots connected by some dark fibrils just below the right end of the filament. Major tick marks are separated by 200″ and the image is rotated so that the filament is horizontal. The white arrow points to disk center (see Fig. 1 in Kuckein, Denker, and Verma, 2014).

found (Kuckein, Denker, and Verma, 2014). On 8 November 2011 the observed filament rotated onto the visible part of the Sun. The eastern-end of the filament erupted on 14 November 2011 as a CME. Caused by a nearby emerging flux region the remainder of the filament broke out on 22 November 2011. The filament vanished completely one day after the CME, which however was not geo-effective.

It is difficult to determine the coordinates of the filament with EUV images, due to different images showing different parts of the filament. The following coordinates are estimated on 16 November 2011 at 12:00 UT. The filament lies approximately between the coordinates (55° N, 50° E) and (14° N, 45° W). It has a length along the great circle of around 100°. In the geometric corrected images the length of the filament is approximately 1000 Mm. Kuckein, Denker, and Verma (2014) observed the filament on 15 November 2011 in Hα, which shows the contours of the filament much clearer (see Fig. 2.8). This image is a composite of ten overlapping slit-reconstructed images observed with the Echelle spectrograph at the Vacuum Tower Telescope (VTT, von der Lühe, 1998) on Tenerife. Kuckein, Denker, and Verma (2014) describe a gap in the filament, which occurs because of the first eruption 15 h before.

To analyze the filament, we use AIA and HMI data which are freely accessible via the SSW IDL library. First, we search the database based on the information about the instrument, the wavelength, the date, and the sample rate of the data. Afterward, we download the data with another routine with specifications of the data repository from which the data should be downloaded. There are nine different repositories in the U.S. and Europe hosting the data. We opted for the National Solar Observatory (NSO) in Tucson, Arizona. The downloaded data are subdivided into two groups: a long-duration and a high-cadence data set.

Long-Duration Data Set

The long-duration data set contains images of two weeks from 8–22 November 2011 with a time resolution of one hour, thus 24 images per day and 336 for the whole time. The images from AIA are in the wavelength bands 171 Å, 193 Å, 211 Å, 304 Å, and 1600 Å; HMI provides magnetograms and filtergrams of the continuum intensity. Additionally, for the 171 Å, 193 Å, and 211 Å wavelength bands a second data set from 1–30 November 2011 is downloaded to create a full-disk tricolor movie (see Section 2.5.2).

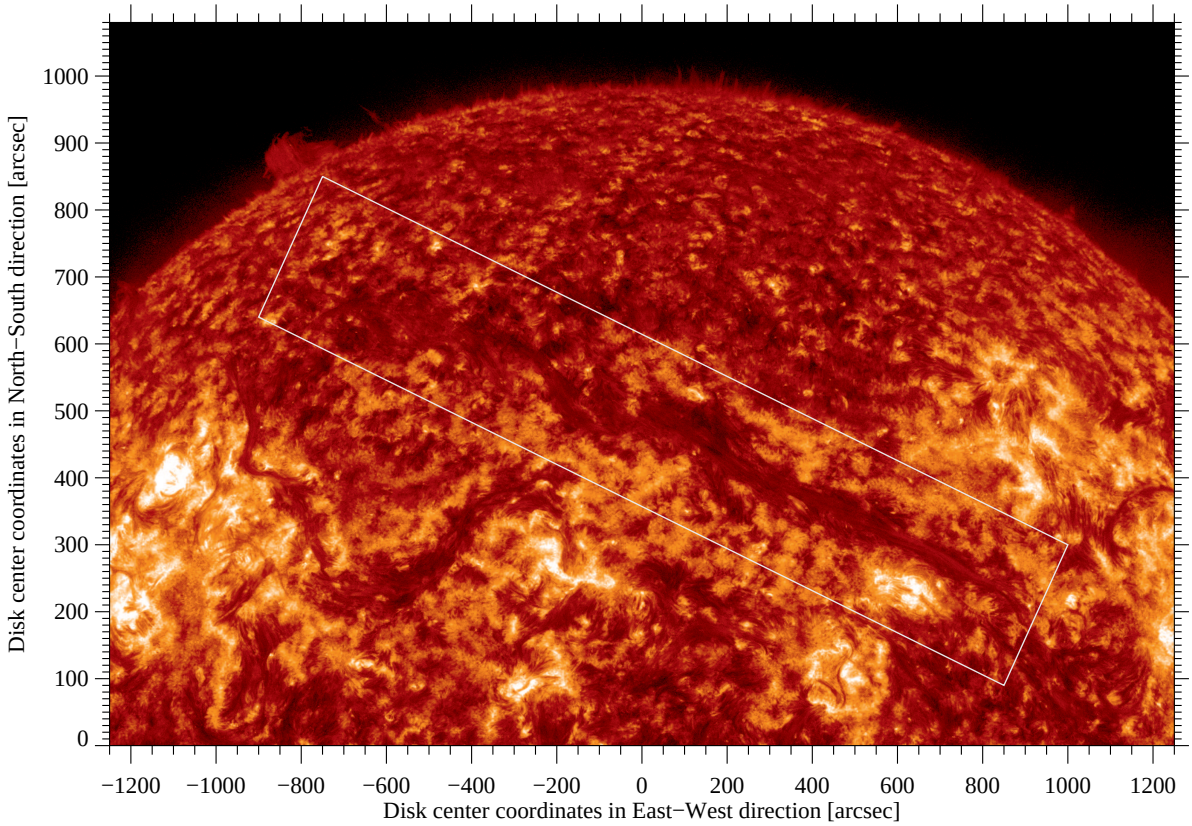

Figure 2.9: Reference image of the filament in the AIA 304 Å wavelength band showing the solar disk before the geometric correction of the image. The image is cropped from a full-disk image and has a size of 2600×1800 pixels. The filament is the dark structure in the white box, and the emerging flux region appears as bright spots at the lower end of the filament (inside the white rectangle). The distances on the Sun are given in seconds of arc.

High-Cadence Data Set

The high-cadence data set contains images of two hours on 16 November 2011 from 11:00 to 13:00 UT with a time resolution of 12 s for the wavelength bands 304 Å, 171 Å, 193 Å, and 211 Å; 24 s for 1600 Å; and 45 s for HMI filtergrams.

2.5.1 Processing the Downloaded Data

Level 1.0 to Level 1.5 Data Conversion

Lemen *et al.* (2012) explains that one simple way to visualize the evolution of solar features is to display the images as movies. In order to accomplish multi-wavelength analysis some more processing is needed. The AIA images were produced with four different telescopes which all have different plate scales and roll angles. To bring them to the same values, we need one processing step. Thus, we produce Level 1.5 data which are not reversible. For HMI data the roll and alignment is the same as for AIA data, but they have another image scale of $0\farcs5$ pixel^{-1}, which needs to be rescaled to match the AIA image scale of $0\farcs6$ pixel^{-1}.

The downloaded data from AIA and HMI are Level 1.0 data. With help of a SSW routine (Brown *et al.*, 2011) the changes described above are applied. The image scale is set to a value of $0\farcs6$ pixel^{-1} (DeRosa and Slater, 2013). The processing step is recorded in the header structure. We use the SSW routine to process full-disk images, but it works also on cropped images and cutouts.

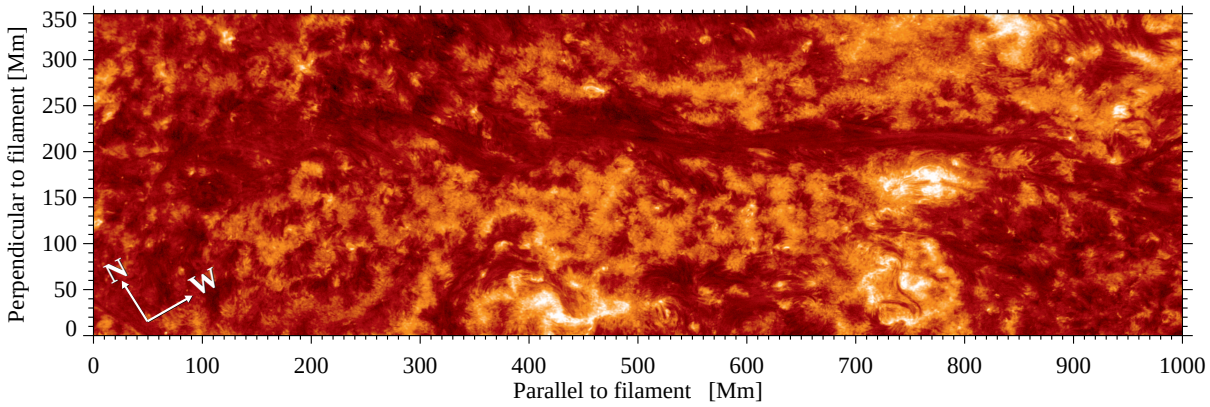

Figure 2.10: Image of the filament on 16 November 2011 in the AIA 304 Å wavelength band after geometric correction and rotation. The image has a size of 3400×1200 pixels. The filament is the dark structure in the middle. At the right end of the filament the emerging flux region is visible as bright spots. The north and west directions are indicated in the lower-left corner. Note that the distances on the Sun are now given in megameters (Mm).

Geometrical Correction of the Filament Images

All images pass through similar processing steps. The starting point is a map, which is a self-describing data structure containing either an image or a magnetogram, and all information regarding observing time, location on the Sun, FOV, etc. These Level 1.5 data have 4096×4096 pixels containing the entire solar disk. The limb darkening is subtracted from the AIA 1600 Å and the HMI continuum images. For this purpose, we compute an average limb-darkening profile. We plot the intensity values I of each pixel as a function of $\mu = \cos\theta$, which is the cosine of heliocentric angle θ, and then we fit a 4$^{\text{th}}$ order polynomial.

$$I(\mu) = c_0 + c_1 \cdot \mu + c_2 \cdot \mu^2 + c_3 \cdot \mu^3 + c_4 \cdot \mu^4 \tag{2.3}$$

This profile still includes dark sunspots and bright points in plage areas. To remove them from the profile a mask of these regions is created. The mask excludes these points, and the procedure is repeated but now with a 1$^{\text{st}}$ order polynomial

$$I(\mu) = c_0 + c_1 \cdot \mu. \tag{2.4}$$

The one-dimensional limb-darkening profile is expanded to two dimensions and subtracted from the AIA and HMI images. Making the rough assumption that small-scale magnetic fields are perpendicular to the solar surface, dividing the magnetograms by μ leads to a coarse geometric correction removing projection effects.

Using AIA 304 Å images, we select a reference map at exactly the time when the Sun's central meridian intersects the filament in the middle, which occurs on 16 November 2011 at 12:00 UT. To save memory and speed up processing we cut out a region of 2600×1800 pixels in the northern hemisphere (see Fig. 2.9). A set of software tools provided by SSW facilitates a straightforward correction of the solar differential rotation. Thus, all data are properly aligned.

Because of the spherical shape of the Sun, we have to implement geometric corrections to get a flat image of the filament in a plane with Cartesian coordinates and square pixels. Therefore, we use Delaunay triangulation (Lee and Schachter, 1980). Here, irregularly-gridded data are arranged in triangles by an algorithm. The surface values are then interpolated with another algorithm onto a regular grid using quadratic polynomial interpolation. This procedure is based on Verma and Denker (2011), who used it for correcting Hinode G-band images. Furthermore, the filament is rotated by 28° to have the filament axis horizontal for easier display (see Fig. 2.10). The images are presented with the standard AIA color coding, which are used to display data on the SDO web services. One pixel has a size of 320 km on the Sun. The images are saved as FITS data and to create movies as Joint Photographic Experts Group (JPEG) files.[3]

[3] www.jpeg.org

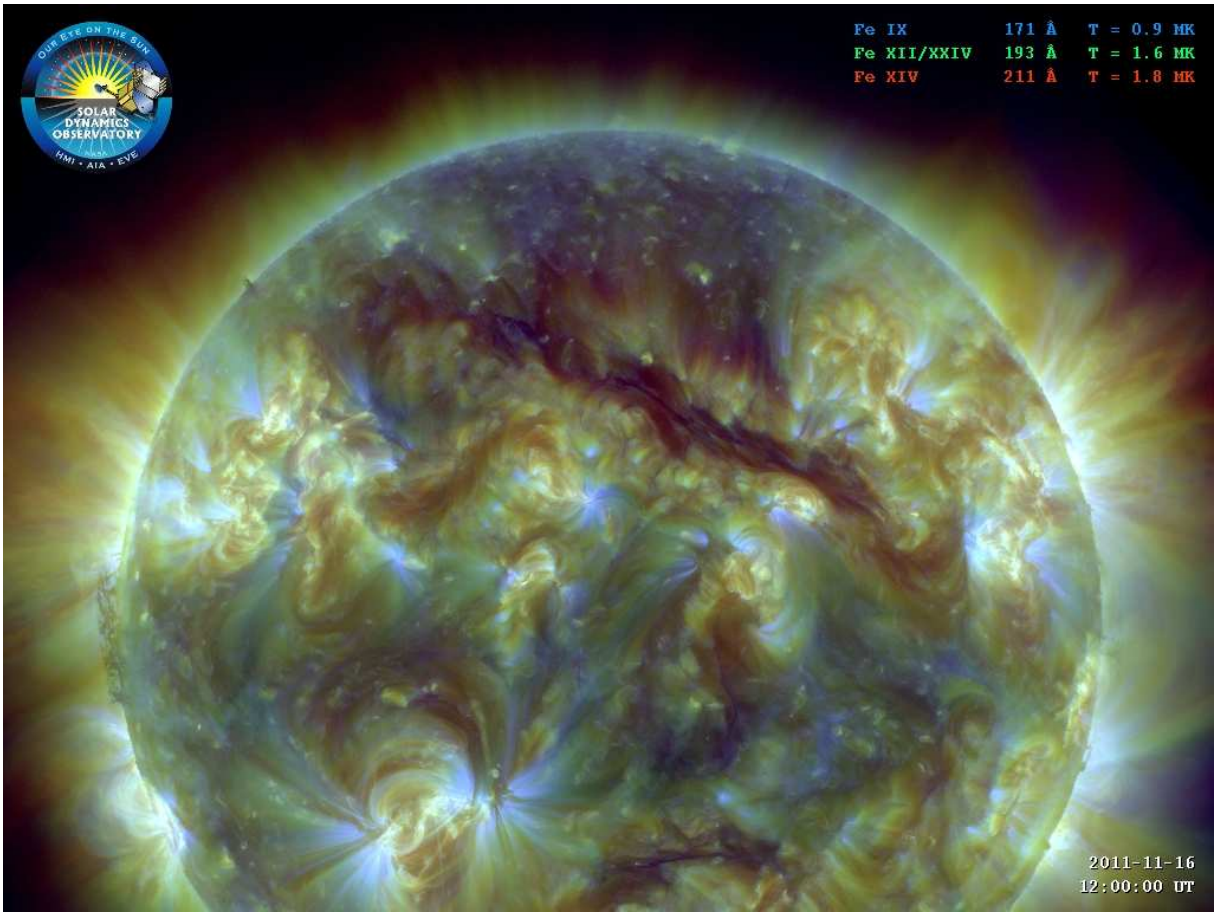

Figure 2.11: False-color image of the giant solar filament on 16 November 2011 at 12:00 UT. The image is composed of three images obtained in the wavelength bands 171 Å, 193 Å, and 211 Å. In the composed image different parts of the corona are highlighted. The blue parts show lower temperatures in the corona, and the yellow parts show the hotter regions. The filament is the dark structure crossing the Sun's central meridian in the northern hemisphere. Filaments have much lower temperatures than the rest of the corona.

2.5.2 Tricolor Images

The images of the wavelength bands 171 Å, 193 Å, and 211 Å were processed as described in Section 2.5.1. After processing each wavelength, we overlay the images to compose a new image (see Fig. 2.11). Every wavelength shows another temperature regime of the corona (see Tab. 2.1). For combining the images, we followed the procedure outlined in DeRosa and Slater (2013). The images show temperatures as colors as we would perceive them: blue for colder regions and yellow for hotter regions in the solar atmosphere. This is a so-called false-color image. The colors match certain temperatures, which are noted in the upper-right corner of Fig. 2.11. The filament itself appears as a dark structure. It resides in the corona and is relatively cool in comparison to the surrounding plasma of the corona. North of the filament is a blue region of quiet corona, a coronal hole, where we look all the way down to the much colder photosphere. The active regions are yellow, showing loop-like structures of hot plasma tracing magnetic fields.

Chapter 3

Results

Prominences are fascinating objects,
abundant in variety, beautiful,
and above all mysterious.

Hirayama (1985)

To better understand the evolution and dynamics of filaments, we have to determine their morphological properties and analyze their proper motions in different layers of the Sun. We determine the chirality properties of the filament because of their importance for eruptive events and their potential to become geo-effective. In the following, two methods for tracking optical flows and a new method for contrast enhancement are introduced, which are used as provided and applied to the data of the giant filament.

3.1 Evolution of the Filament

We study the evolution of the filament with the long-duration data set. On 8 November 2011 the filament rotated onto the visible part of the Sun and vanished completely about two weeks later on 23 November 2011. It is not known, how long the filament existed before. First, we study the magnetic field evolution with HMI magnetograms, then the photospheric evolution with HMI continuum images, and last the layers of the corona with the different AIA wavelength bands.

Evolution of the Magnetic Field

The filament lies on top of a polarity inversion line (PIL) which separates the two magnetic polarities. The HMI magnetograms (see Fig. 3.2) show that the observed filament has the positive polarity (white) in North-West direction above the filament and the negative polarity (black) in the South-East direction below the filament. One rotation period earlier there was a large active region and we assume that the remaining trailing flux of this active region is the magnetic flux above and below the PIL.

On 14 November 2011 an emerging flux region (EFR) appeared at the lower right end of the filament and vanished on 19 November 2011. An emerging flux region is the signature of new flux emergence from the convection zone into the solar atmosphere. It appears as two features with opposite polarities (Thornton and Parnell, 2011). This EFR is labeled as active region NOAA 11349. The negative polarity of the EFR is East and the positive polarity is West (see Fig. 3.3).

Evolution of the Photosphere

We see sunspots appearing from 14–19 November 2011 in the EFR. The sunspots are of $\alpha\gamma$- or $\beta\gamma$-type. The sunspots appeared as a bipolar group with the polarities separating over time. At no time, there were more than three spots in either the leading or trailing part of the active region, and their lifetime was approximately one day. With the decay of the emerging flux region on 19 November 2011 also the sunspots vanished. Furthermore, we observe around the filament channel many plage regions.

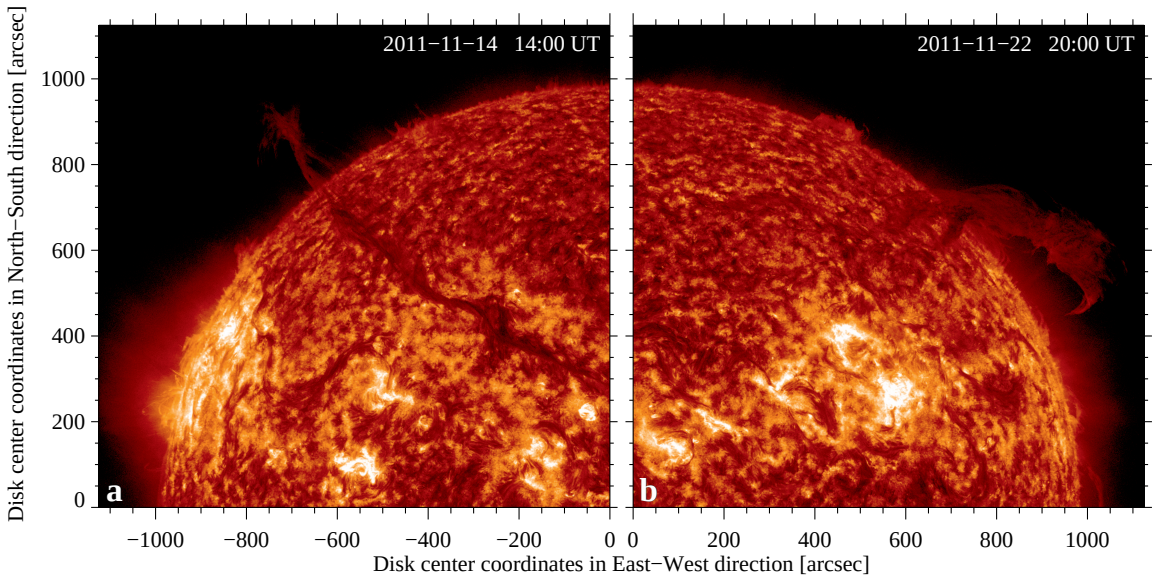

Figure 3.1: Two eruptions of the filament occurred during its life-time. (a) One part of the filament erupted on 14 November 2011 at 14:00 UT. Because of an eruption in the emerging flux region NOAA 11349 on 19 November 2011, one half of the remaining filament moved upward and vanished from the solar surface. This eruption caused also the instability of the rest of the filament whereupon (b) the filament lifted off on 22 November 2011 at 20:00 UT and vanished completely on 23 November 2011 at around 7:00 UT.

Evolution in the Corona

In the corona, we observe the filament's plasma itself. The filament appears as dark structures because the plasma is much colder than the surrounding coronal plasma. Again, the occurrence and decay of the EFR is observable. On 17 November 2011 at around 17:00 UT a brightening occurred in the plage region below the EFR. It connected both the plage region and the EFR for a short time period. A flare was not reported for this time.[1]

We observe two eruptions during the lifetime of the filament. The first eruption started on the 13 November 2011 at around 12:00 UT with the uplifting of the plasma and on 14 November 2011 at around 21:00 UT the filament erupted as a non geo-effective CME (see Fig. 3.1, left panel). Thereby, a gap develops in the filament, which is visible in the Hα images (see Fig. 2.8, left end of the filament). The second eruption can be separated into two parts. On 20 November 2011 at around 16:00 UT the emerging flux region destabilized the filament and caused an eruption, where one half of the filament blew up as a non-geo-effective CME. This eruption spreads as a shock-wave in the neighboring region. As a consequence, a flare was released by active region NOAA 11350 on 21 November 2011 at 7:16 UT.[1]The eruption caused also the instability of the rest of the filament whereby it lifted off, vanishing completely from the solar surface on 23 November 2011 at around 7:00 UT (see Fig. 3.1, right panel).

Chirality of the Filament

The chirality patterns of a filament is important, because they give information about the helicity of the upcoming CMEs. To determine the chirality of the filament we have to determine the direction of the barbs. Therefore, we have a look at the Hα image in Fig. 2.8. The positive polarity is North-West of the filament and the negative South-East of it. Viewed from the positive-polarity side of the filament the barbs are right-bearing (see feature 2 in Fig. 1.4). This confirms the assumption that right-bearing barbs are dominant on the northern hemisphere as described in Martin (1998a,b). Because dextral filament channels have right-bearing barbs, we can assume that our filament is also dextral. To confirm the helicity of the arcades, we view a movie of the long-duration data set of the AIA 171 Å wavelength band. It was not possible to determine the helicity of the CME at the end of the filament's lifetime, because it appeared too close to the solar limb. But we expect a left-helical CME, which is typical for a dextral filament.

[1] solarmonitor.org

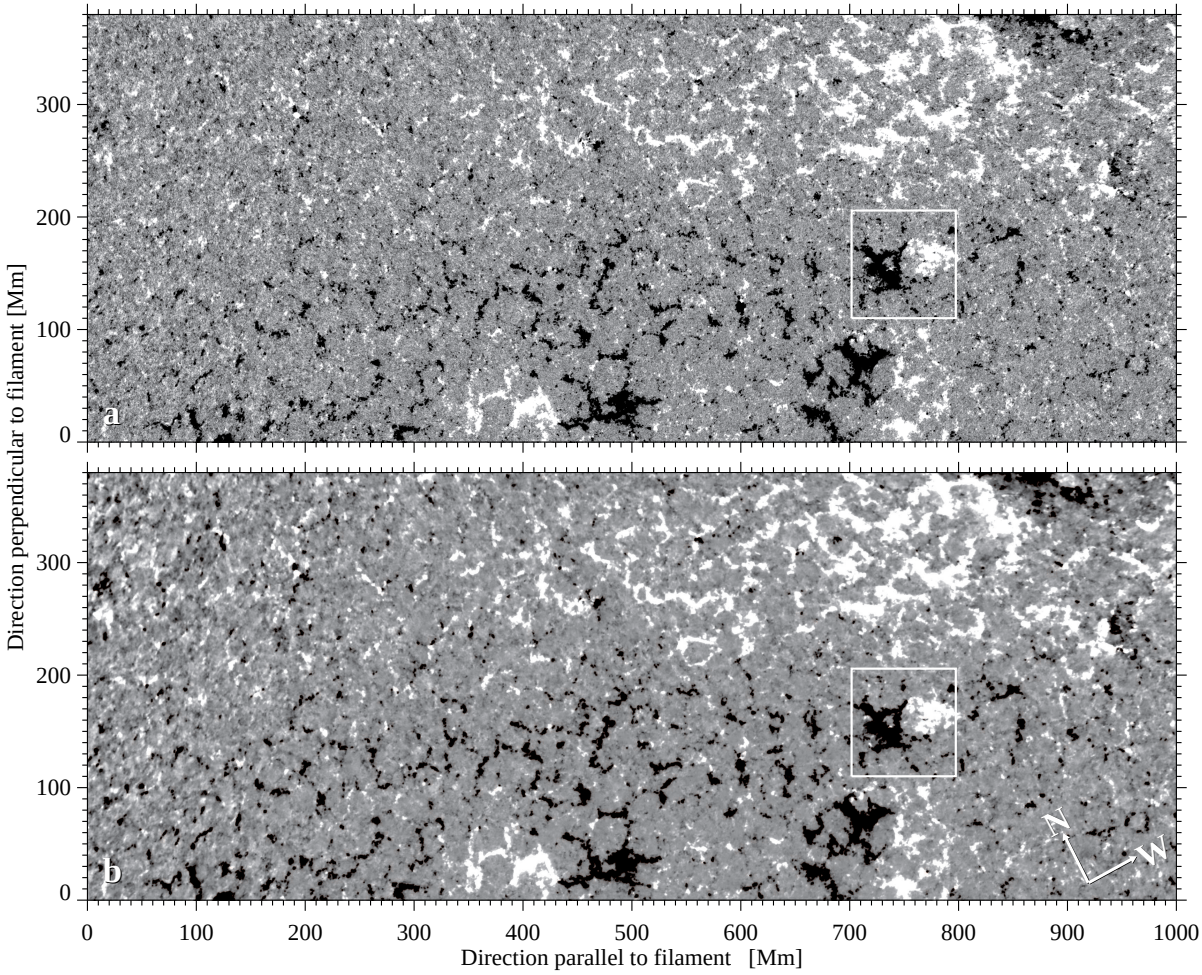

Figure 3.2: The emerging flux region with a FOV of 960×380 Mm. (a) Reference magnetogram on 16 November 2011 at 12:00:28 UT and (b) average of 160 magnetograms. Both images are clipped at ±25 G. The white square shows the emerging flux region. An enlarged view is presented in Fig. 3.3.

3.2 Dynamics of the Filament

To analyze the dynamics of the filament we determine the velocity in different layers of the solar atmosphere with two different methods: local correlation tracking (LCT) and differential affine velocity estimator (DAVE). Therefore, we use the high-cadence data set with a temporal duration of two hours on 16 November 2011. First of all, we inspect the deep magnetogram, in which weak magnetic fields are easier to discern and the noise is much reduced.

3.2.1 Deep Magnetogram of the Filament

We take the average of the magnetograms from the high-cadence data set to create a deep magnetogram. Therefore, we sum the 160 magnetograms of the two hour time-series and divide them by the total number n of images. In the resulting deep magnetogram (see Fig. 3.2b) the noise is reduced by a factor of $\sqrt{n} = 12.6$. In the deep magnetogram more details of the magnetic structure are recognizable. The noise is reduced, and also tiny magnetic field structures become noticeable. Especially in the upper-left part of Fig. 3.2a, the noise is distinctive. By averaging the image, the different polarities can be now more easily differentiated. Furthermore, the PIL is better recognizable between the positive and negative polarity parts of the filament. The overall impression is that the magnetic field structure is smoothed. As in the quiet-Sun regions of the magnetogram the noise in the EFR is reduced and the deep magnetogram gives a smoothed impression (see Fig. 3.3).

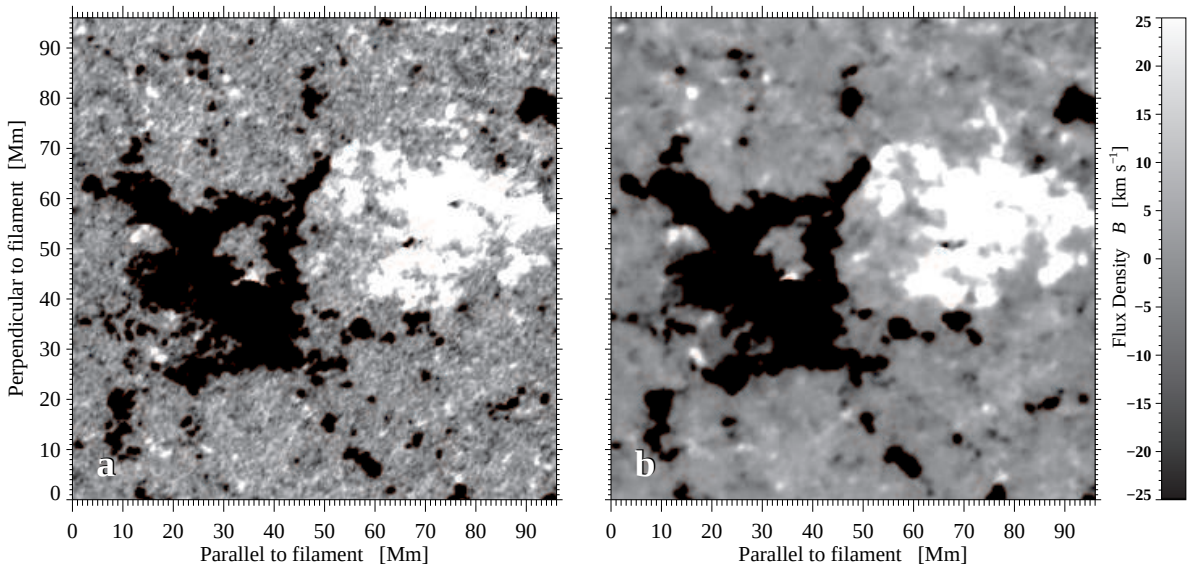

Figure 3.3: (a) Reference magnetogram of the emerging flux region on 16 November 2011 at 12:00:28 UT and (b) deep magnetogram of the EFR. Both magnetic fields are clipped at ±25 G. In the image, the noise is well controlled. The FOV has a size of 96 Mm×96 Mm.

3.2.2 Local Correlation Tracking

Getting information about the horizontal proper motions is important while analyzing the dynamics of solar structures. There are two main methods to measure the horizontal velocity flows: feature tracking (FT) and LCT (November and Simon, 1988; Verma and Denker, 2011). The first method follows the footprints of individual features in the image. Feature tracking has three main steps: segmentation – identify pixels which belong to any object, labeling – identify pixels which belong to the same object and labels them, and identification of the traced objects – find relationships between the objects in the first and second image of a time-series (Strous, 1995). The second method is LCT, where the localized cross-correlation between two images of a time-series yields a displacement vector (November and Simon, 1988). We use the LCT algorithm for our high-cadence data set to determine the horizontal flow velocities of the plasma in the filament. Later, we compare the results with the technique of Schuck (2006), which tracks optical flows in magnetograms with DAVE.

Leese, Novak, and Clark (1971) developed LCT for tracking clouds, and November and Simon (1988) implemented the algorithm for solar physics. Verma (2013) adapted the algorithm to Hinode G-band images using sub-images with a size of 32×32 pixels (2560 km×2560 km). We applied the algorithm to our data set with a sub-image size of 16×16 pixels which corresponds to 5120 km×5120 km. Verma and Denker (2011) studied the influence of different sub-image sizes on the LCT results and came to the conclusion, that there are only small changes in the results for sub-images with sizes of 2560 km×2560 km and 5120 km×5120 km. Only the computing time was smaller for the smaller sub-images.

The following description is based on the work of Verma and Denker (2011) and November and Simon (1988). First, a high-pass filter is applied to suppress gradients related to structures smaller than granules (Verma and Denker, 2011). The high-pass filter is a Gaussian with a Full-Width-at-Half-Maximum (FWHM) value of 2000 km (6.5 pixels). For the sub-image we use the notification $i(x',y')$ with the coordinates x' and y' related to the sub-image. The Gaussian kernel in the high-pass filter becomes

$$g(x',y') = \frac{1}{2\pi\sigma^2} e^{-\frac{r(x',y')^2}{2\sigma^2}}, \tag{3.1}$$

where $\sigma = {}^{\mathrm{FWHM}}/_{2\sqrt{2\ln 2}}$ and $r(x',y') = \sqrt{(x'^2+y'^2)}$. Thereby, a background image can be computed with a low-pass filter

$$i_{\mathrm{low}} = i(x,y) \otimes g(x',y'), \tag{3.2}$$

where $\otimes$ denotes a convolution of the Gaussian g and the original image i. The high-pass filter is then computed as

$$i_{\text{high}} = i(x,y) - i_{\text{low}}. \tag{3.3}$$

The underlying assumption for the LCT algorithm is the constant velocity profile (Schuck, 2005), which is implemented in the cross-correlation. The main part of the LCT algorithm is the cross-correlation $c_l(x,y,x',y')$ over 16×16 pixels region centered on the coordinates (x,y) of each pixel of the image pair $i_l(x,y)$ and $i_{l-1}(x,y)$ (Verma, 2013).

$$c_l(x,y,x',y') = \Re\{\mathscr{F}^{-1}[\mathscr{F}(i_{l-1}(x,y,x',y',)g(x',y')) \cdot \mathscr{F}^*(i_l(x,y,x',y')g(x',y')]\}d(x',y')), \tag{3.4}$$

where $g(x',y')$ denotes a weighting function also serving as an apodising window. It is the same Gaussian as previously used in the high-pass filter kernel. We need only the real part $\Re$ of the cross-correlation. The $\mathscr{F}$ denotes the fast Fourier transform (FFT), $\mathscr{F}^{-1}$ the inverse of it, and $\mathscr{F}^*$ refers to the complex conjugate of $\mathscr{F}$. Additionally, we define the mask $d(x',y')$. The mask denotes, that the maximum of the cross-correlation is forced to be within a distance of $c_{s,\text{lim}} = 6$ pixels from its center.

$$d(x',y') = \begin{cases} 1: & r(x',y') \leq c_{s,\text{lim}} \\ 0: & r(x',y') > c_{s,\text{lim}} \end{cases} \tag{3.5}$$

The photospheric speed of sound is $c_s \approx 8$ km s^{-1}. We have a time interval of around 90 s, in which the plasma would travel 720 km, which corresponds to 2.25 pixels. Thus a maximum value of $c_{s,\text{lim}} = 6$ pixels is justified (Verma, 2013).

November and Simon (1988) used ground-based observations, thus they had to reduce the atmospheric seeing effects by averaging the cross-correlation in time. We have satellite observations, which are not affected by atmospheric seeing effects. However, averaging is still needed, if one is interested in the persistent flow field and not in the evolution of individual fine structure.

We use the LCT algorithm primarily for two different data sets: the HMI continuum images and the AIA 1600 Å images. After enhancing the AIA 171 Å images with a new method, called NAFE (see Section 3.2.4), we use the LCT algorithm again to determine the horizontal proper motions in the corona. We compare our results with the results from DAVE, which are based on HMI magnetograms. All images have the same size of 3400×1200 pixels (1088 Mm×384 Mm). The images have a time cadence $\Delta t = 12$, 24, and 45 s for the AIA 171 Å, 1600 Å, and HMI continuum images, respectively. The time cadence Δt in the LCT algorithm should be comparable so we define $\Delta t' = n \cdot \Delta t$, with $n = 2$, 4, and 8 in our case; $\Delta t' = 96$ s for the AIA images, and $\Delta t' = 90$ s for the HMI images. If the time cadence is too long, the features will evolve too much for the algorithm to track them (Verma and Denker, 2011). The Gaussian kernel has a size of 16×16 pixels (5120 km × 5120 km) with a FWHM = 6.25 pixels corresponding to 2000 km in all three cases. This size was tested in Verma and Denker (2011) and has shown no significant differences to the smaller kernel of 2560 km ×2560 km used there. A kernel with a smaller FWHM produces more detailed flow maps. Because of the large image scale of the SDO data of 1 pixel = 320 km, we choose a small FWHM.

Photospheric Velocities from HMI Continuum Images

The HMI continuum images show the photosphere of the Sun, where the sunspots are located. In the high-cadence data set with a duration ΔT = 120 min are 160 images with a time cadence of $\Delta t = 45$ s. In the LCT algorithm, we use a time cadence of $\Delta t' = 2 \cdot 45$ s = 90 s. Thus, we obtain a mean velocity for the whole FOV of v_{mean} = (0.44 ± 0.24) km s^{-1} and a maximum value of v_{max} = 3.21 km s^{-1}. In Fig. 3.4a the original HMI continuum image on 16 November 2011 at 12:00 UT and in Fig. 3.4b the LCT velocity map over two hours are shown. The darker colors show the regions with smaller velocities, and the red regions correspond to high velocities. In the middle of the image, where the filament is located, the velocities can reach a maximum velocity of v_{max} = 3.21 km s^{-1} in a small localized area. At the left edge of the image, we measure high velocities. Because our FOV is large, we see the regions close to the solar limb. This is the reason, why we see a combination of different effects, which produce these

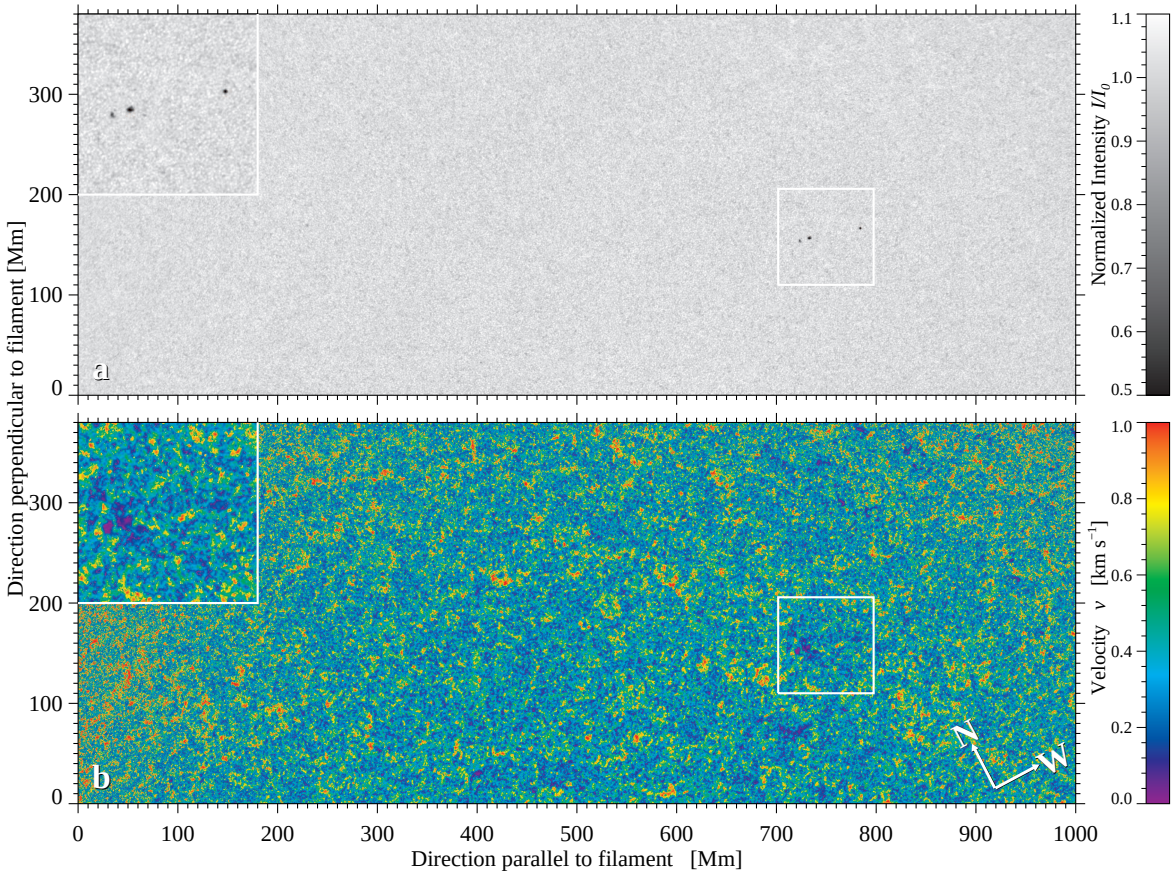

Figure 3.4: (a) HMI continuum image and (b) LCT velocity map based on HMI continuum images. In the upper-left corner, we present an enlargement of the EFR inside the white square with a size of 96 Mm×96 Mm.

high velocities. Among others, we have still projection effect of the 2nd order; we accumulate small mistakes in the differential-rotation correction, which are add up at the edge; border pixel cover a greater area, providing a reduced spatial resolution and consequently noisier velocity estimates; and upward and horizontal motions become intermingled at the border.

High values of the velocity are only encountered in localized regions, which could may be the footpoints of the filament. The filament reaches from the corona down into the photosphere, where the footpoints are located.

In the upper-left corner of Fig. 3.4, we have an enlargement of the EFR. In the continuum image, we can see three sunspots. In the velocity map we see that the velocity is nearly zero where the sunspots are located. The strong magnetic field of the sunspots suppresses the convective energy transport leading to reduced flow speeds. Around the sunspots are regions with high velocities, which are indicative of the moat flow (Pardon, Worden, and Schneeberger, 1979). The maximum velocity in this FOV is $v_{\mathrm{max,EFR}}$ = 1.20 km s^{-1}, and the mean velocity is $v_{\mathrm{mean,EFR}}$ = (0.38 ± 0.20) km s^{-1}.

Velocities of the Upper Photosphere, Lower Chromosphere, and Transition Region from AIA 1600 Å Images

The AIA 1600 Å images show the transition region, the lower chromosphere, and the upper photosphere of the Sun. In the high-cadence data set with a duration ΔT = 120 min are 300 images with a time cadence of $\Delta t = 24$ s. In the LCT algorithm we use a time cadence $\Delta t' = 4 \cdot 24$ s = 96 s. We obtain a mean velocity of v_{mean} = (0.84 ± 0.51) km s^{-1} and a maximum velocity of v_{max} = 4.90 km s^{-1}. Figure 3.5 shows the original AIA 1600 Å image on 16 November 2011 at 12:00 UT and the corresponding LCT velocity map averaged over two hours. The smaller velocity values are located in regions with EUV brightenings, which are associated with the magnetic fields of plage regions and the supergranular network. The flow map does not provide any indication pointing to the presence of a filament within the FOV.

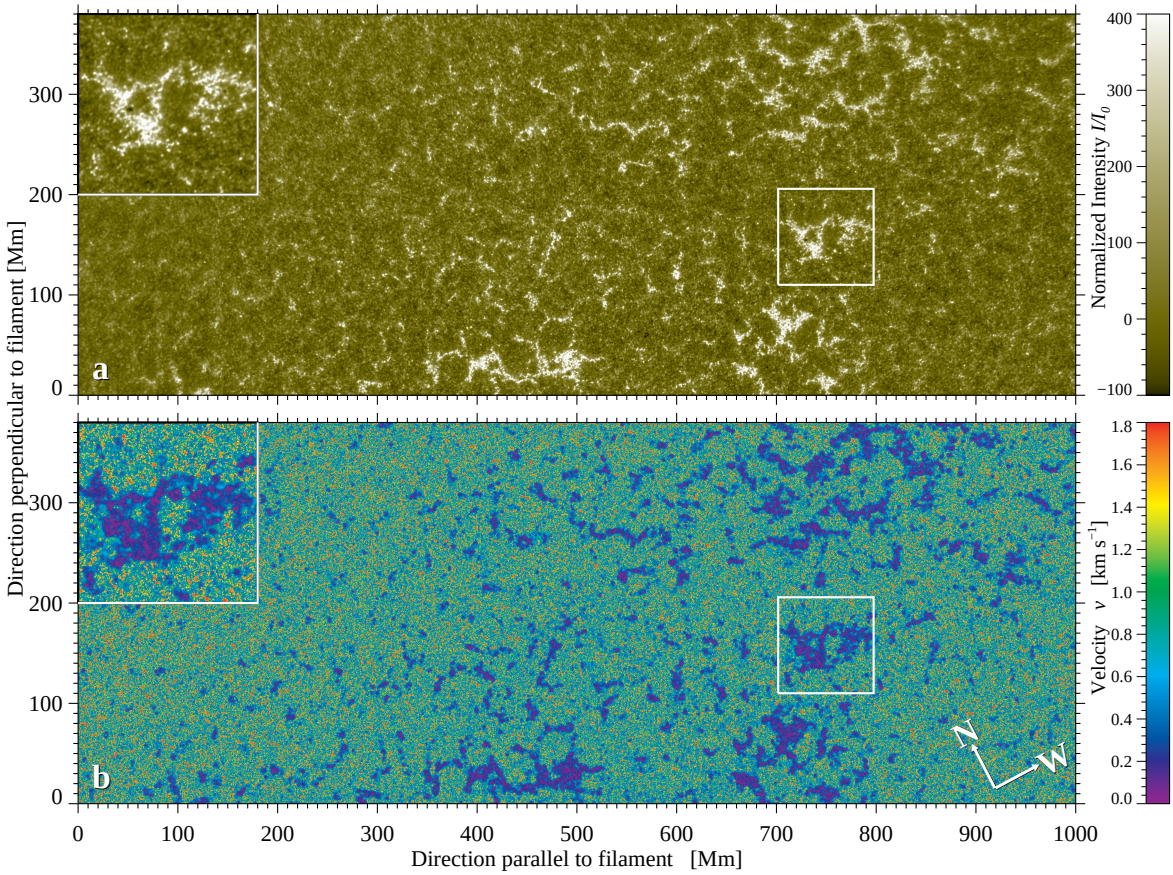

Figure 3.5: (a) AIA 1600 Å reference image and (b) corresponding LCT velocity map. In the upper-left corner, we present an enlargement of the EFR inside the white square with a size of 96 Mm×96 Mm.

In the upper-left corner of Fig. 3.5, we have an enlargement of the EFR. The EFR appears bright in the AIA 1600 Å wavelength band, which also shows the three sunspots as tiny dark spots. The velocity map shows that in this region the velocities are very small. In the surroundings of the EFR, however, are small areas with high velocities up to $v_{\mathrm{max,EFR}}$ = 3.80 km s^{-1}. The whole FOV has a mean velocity $v_{\mathrm{mean,EFR}}$ = (0.69 ± 0.49) km s^{-1}. The flow-speed structure of the EFR is similar to its magnetic field structure. Both the AIA 1600 Å images and the HMI magnetograms (see Fig. 3.2a) show similar structures in the upper photosphere/transition region and photosphere, respectively.

3.2.3 Differential Affine Velocity Estimator

The DAVE (Schuck, 2005, 2006) uses an affine velocity profile, instead of a constant velocity profile as the LCT algorithm. The DAVE algorithm uses magnetograms to track the magnetic field proper motion by comparing the temporal and spatial derivatives of the magnetic field. By assuming a constant velocity profile any contraction, dilation, or rotation of the magnetic fluid in the sample window is neglected. In this method an accurately representation of the magnetic induction equation is used. Schuck (2006, 2005) shows that DAVE achieves better results for magnetograms than the LCT algorithm. Furthermore, the computation time is significantly lower than for LCT. Chae and Sakurai (2008) presented a non-linear variation of the DAVE method and called it consequently NAVE. To illustrate the underlying physics of DAVE, we present the algorithm as shown in Schuck (2005, 2006). We apply the existing method as provided to our data set.

The DAVE method assumes an affine velocity profile as well as applying the magnetic field equation. Schuck (2006) starts with the MHD magnetic induction equation

$$\frac{\partial \mathbf{B}}{\partial t} = \nabla \times (\mathbf{v} \times \mathbf{B}) - \frac{c^2}{4\pi} \nabla \times \left(\frac{1}{\sigma} \nabla \times \mathbf{B} \right), \tag{3.6}$$

to develop the DAVE algorithm. The boldfaced variables denote vectors or matrices. The equation is simplified by assuming perfect conduction in the photosphere with $\sigma_p \to \infty$. The normal component of the magnetic induction equation $\mathbf{B}_n$ becomes

$$\frac{\partial \mathbf{B_n}}{\partial t} + \nabla_t \cdot (\mathbf{B_n}\, \mathbf{u_F}) = 0. \tag{3.7}$$

In this relation, $\mathbf{u}_F$ is the velocity of the magnetic footpoints tangential to the photospheric surface. It is difficult to determine the magnetic footpoint velocity $\mathbf{u}_F$. Therefore, we can assume that $\mathbf{B_n}\, \mathbf{u_F} \sim \mathbf{B_n}\, \mathbf{u}$, where $\mathbf{u}$ is the optical flow field. This is possible because of the Helmholtz decomposition (Schuck, 2006)

$$\mathbf{B_n}\, \mathbf{u_F} \sim \mathbf{B_n}\, \mathbf{u} = -(\nabla_t \phi + \nabla_t \psi \times \hat{\mathbf{n}}), \tag{3.8}$$

where the scalar ϕ is the inductive stream function and scalar ψ is the electrostatic potential. Thus, we get a continuity equation (for $\mathbf{B}_n \neq 0$)

$$\frac{\partial \mathbf{B_n}}{\partial t} + \nabla_t \cdot (\mathbf{B_n}\, \mathbf{u}) = 0. \tag{3.9}$$

The affine velocity profile (Schuck, 2005, 2006) is given as

$$\mathbf{u}(\mathbf{x}) = \mathbf{u_0} + \mathbf{W} \cdot \mathbf{x}, \tag{3.10}$$

where $\mathbf{u_0} = U_0 \hat{\mathbf{x}} + V_0 \hat{\mathbf{y}}$ represents the velocity field at $\mathbf{x} = \chi$, and the gradient of the flow within the subregion and the constant values U_x, U_y, V_x, and V_y:

$$\mathbf{W}(\mathbf{P}) = \nabla \mathbf{u}(\mathbf{x})|_{\mathbf{x}=\chi} = \begin{pmatrix} U_x & U_y \\ V_x & V_y \end{pmatrix} \tag{3.11}$$

The tensor $\mathbf{W}(\mathbf{P})$ describes the local shear flows. Schuck (2006) considers now the Lagrangian trajectory $\mathbf{R}$ of a fluid element in nonuniform time-invariant flow

$$\frac{\partial \mathbf{R}(t; \mathbf{x_i}, t_i)}{\partial t} = \mathbf{v}[\mathbf{R}(t; \mathbf{x_i}, t_i)], \tag{3.12}$$

where the Lagrangian velocity is the Eulerian velocity $\mathbf{v}(\mathbf{x})$ at the location of the fluid element. In the neighborhood $\mathbf{x} = \chi$ the velocity profile $\mathbf{u}_\chi \sim \mathbf{v}$ and the continuity equation can be written as

$$\frac{\partial \mathbf{R}_\chi(t; \mathbf{x_i}, t_i)}{\partial t} = \mathbf{u_0} + \mathbf{W} \cdot [\mathbf{R}_\chi(t; \mathbf{x_i}, t_i) - \chi]. \tag{3.13}$$

The Lagrangian trajectory is then defined as

$$\mathbf{R}_\chi(t; \mathbf{x_i}, t_i) = \chi + \mathbf{L} e^{\lambda (t - t_i)} \mathbf{L}^{-1} \cdot (\mathbf{x_i} - \chi) + \left[\mathbf{L} e^{\lambda (t - t_i)} \mathbf{L}^{-1} - \mathbf{I}\right] \mathbf{W}^{-1} \cdot \mathbf{u_0}, \tag{3.14}$$

where $\mathbf{R}_\chi$ is the trajectory around $\mathbf{x} = \chi$,

$$\mathbf{L} = \begin{pmatrix} \frac{\lambda_+ - V_y}{V_x} & \frac{\lambda_- - V_y}{V_x} \\ 1 & 1 \end{pmatrix}, \tag{3.15}$$

and

$$\lambda = \mathbf{L}^{-1} \mathbf{W}\, \mathbf{L} = \begin{pmatrix} \lambda_+ & 0 \\ 0 & \lambda_- \end{pmatrix}, \tag{3.16}$$

with the eigenvalues

$$\lambda_\pm = \frac{1}{2} \left[U_x + V_y \pm \sqrt{4 U_y V_x + (u_x - v_y)^2} \right]. \tag{3.17}$$

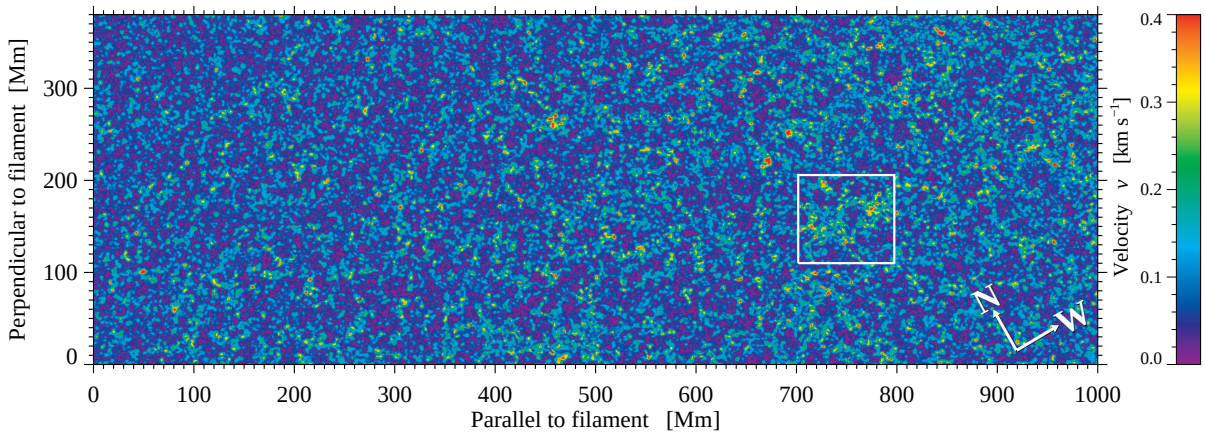

Figure 3.6: Velocity map of the photosphere created with the DAVE algorithm. The maximum value of the velocity is 0.89 km s^{-1}. The white square shows the location of the EFR.

The exact solution of the continuity equation for an affine velocity profile (Schuck, 2005) is

$$I(\mathbf{x},t) = e^{-(U_x+V_y)\Delta t} I[\mathbf{R}(t;\mathbf{x},t+\Delta t),t]. \tag{3.18}$$

The correlation integral to incorporate the continuity equation, by determining the motion with minimized sum-of-squared differences (SSD) in intensity of the two successive images (Schuck, 2005, 2006) is given as

$$C_{\mathrm{SSD}}(\chi,t,\Delta t;\mathbf{M}) = \int d^2x\, w(\chi-\mathbf{x})\{I(\mathbf{x},t+\Delta t) - e^{-(U_x+V_y)\Delta t} I[\mathbf{R}_\chi(\tau;\mathbf{x},t+\Delta t),t]\}^2, \tag{3.19}$$

where $\mathbf{M} = (U_0, V_0, U_x, V_x, U_y, V_y)$ is the vector of the output parameters. They describe the properties of the local affine velocity profile.

For the algorithm, we need input parameters, which contain the structure of the vector magnetic field, e.g., the magnetic field component in z-direction B_z perpendicular to the solar surface and its temporal and spatial derivatives dB_z/dt, dB_z/dx, and dB_z/dy. The temporal derivative is based on a five-point-stencil with a 15-minute time cadence $\Delta t'$. The time cadence $\Delta t'$ is given by the parameter h = 20 and the time cadence $\Delta t' = h \cdot \Delta t = 20 \cdot 45$ s = 15 min. The time cadence also defines the time interval $\Delta T = 60$ min. In the parameter study, we vary the time cadence by changing the parameter h and the time interval ΔT. The spatial derivative is computed with the Scharr (2007) operator and then convolved with a sampling window of 11 pixels (Balthasar *et al.*, 2014). The output parameters of the routine are U_0, which is the flux transport velocity in x-direction and V_0, which is the flux transport velocity in y-direction. We derive the mean velocity v from the parameters U_0 and V_0 as

$$v = \sqrt{U_0^2 + V_0^2}. \tag{3.20}$$

Velocities of the Magnetic Field from HMI Magnetograms

As for the LCT algorithm we create a velocity map with the DAVE algorithm. The velocity map shows the magnetic flux transport velocity in the photosphere (see Fig. 3.6). The maximum velocity $v_{\mathrm{max}} = 0.89$ km s^{-1}, and the mean velocity is $v_{\mathrm{mean}} = (0.084 \pm 0.063)$ km s^{-1}.

In Fig. 3.7 we create an overlay of the AIA 304 Å image of the filament (grayscale), the magnetic field (red or blue for positive or negative polarities), and the velocities (displayed as arrows). The arrows have different length and colors representing the flow speed. The long, red arrows represent regions with high velocities, whereas the short, blue arrows stand for smaller velocities. Around the filament's spine the velocities are high, whereas outside the filament the velocities have smaller values. The EFR on the lower right-side image is clearly visible, because of the strong magnetic field structure in blue and red. The velocities were computed for the reference image of the time-series, i.e., the velocity

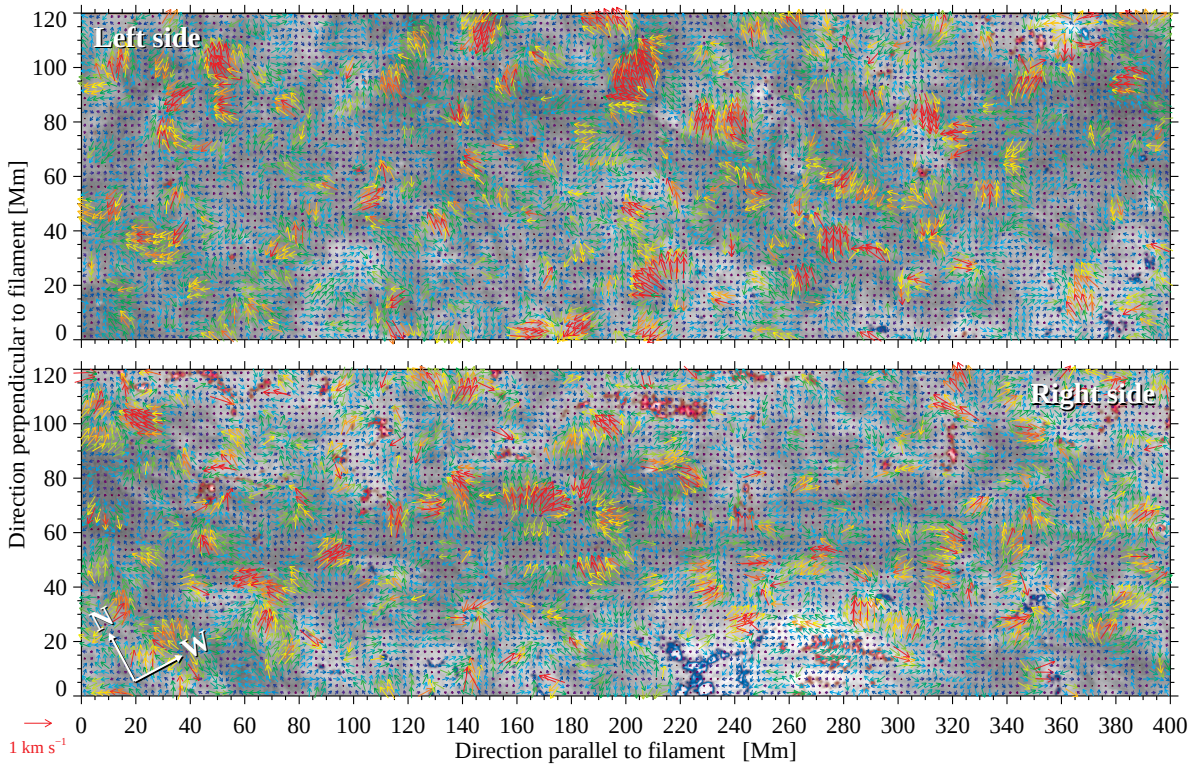

Figure 3.7: Image composed of the filament from the AIA 304 Å wavelength band (black and white structure in the background), the magnetic field (red and blue structures for positive and negative polarities), and the velocity of the filament presented as arrows. The long red arrows represent high velocities of more than 2 km s^{-1}. The red arrow in the lower-left corner represents corresponds to a flow speed of 1 km s^{-1}. We split the filament into two parts whereby each has a size of 400 Mm×120 Mm. The emerging flux region is clearly visible in the lower part of the bottom panel as red and blue structure.

values are not averaged over the full 2-hour duration of the time-series. Thus, the velocities reach higher values. The maximum value for this region is $v_{\mathrm{max}} = 1.24$ km s^{-1}, and the mean value is $v_{\mathrm{mean}} = (0.29 \pm 0.16)$ km s^{-1}.

Velocities of the Emerging Flux Region

Now, we will have a closer look at the EFR. Therefore, we display the EFR in a small region-of-interest (ROI) of 96×96 Mm. We present in Fig. 3.8 the magnetic field with the velocities shown as arrows and the velocity map for the time interval ΔT = 60 min. The maximum velocity for the EFR is $v_{\mathrm{max}} = 0.52$ km s^{-1}, and the mean velocity is $v_{\mathrm{mean}} = (0.09 \pm 0.07)$ km s^{-1}. There is a divergent flow at the edge of the sunspot in the negative polarity part. Some convergent flows, on the other side of the divergent flow, are bypassing the strong magnetic field structure. Another divergent flow, inside the positive-polarity part, is reaching the maximum velocity values.

In the next part, we will study the dependence of the velocity on the time interval ΔT and the time cadence $\Delta t'$. For the time interval we choose the values ΔT = 15, 30 60, and 90 min, and for the time cadence we change the parameter h by using the values h = 2, 5, 10, 15, and 20 to arrive at time intervals of Δt = 1.5, 3.75, 7.5, 11.25, and 15 min, respectively.

We compute the DAVE flow speed maps for the EFR region for the different time cadences. Afterward, we sum for each time interval the flow maps and build the average including the reference map at 12:00 UT. The data sets with a h-value of 15 and 20 contain 100 and 80 images, thus it is not possible to compute an average over 90 min, which corresponds to 120 images. Therefore, we get no data. In Fig. 3.9 are the computed flow maps with the mean velocities with their standard deviations σ_v, and in Tab. 3.1 are the mean and maximum value for each flow speed map. This shows that the highest velocities are obtained with a small time cadence $\Delta t'$ and a small time interval ΔT.

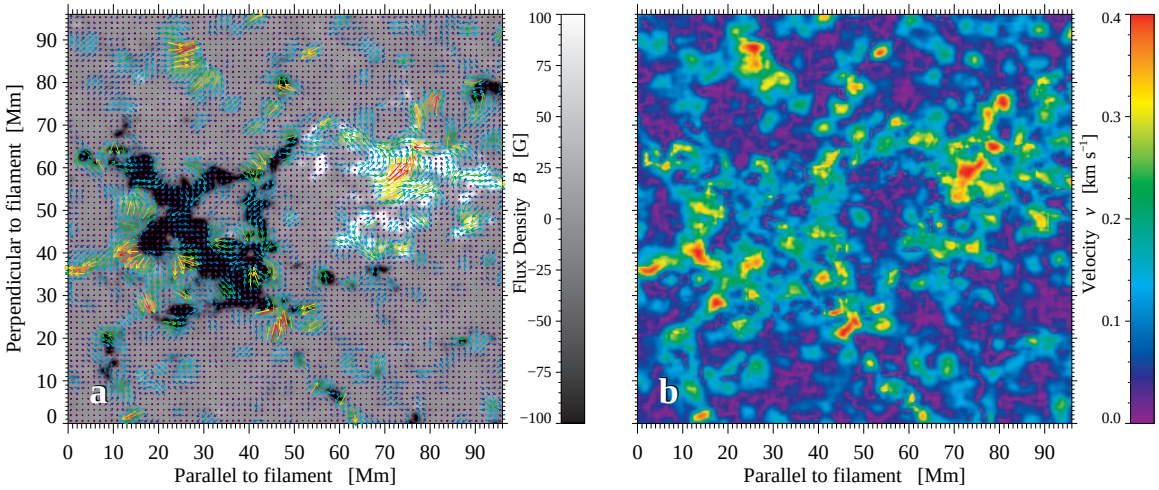

Figure 3.8: Magnetic field and velocity map of the EFR. (a) The magnetic field with superposed flow vectors for the time interval of ΔT = 60 min and (b) the flow speed map for the EFR with velocities up to 0.4 km s^{-1}.

Table 3.1: Dependence of the time interval ΔT, for the average flow map and the spacing of image h in time based on the maximum and mean values for the velocity $v_{\max}$ and v_{mean}. The mean velocity is given along with its standard deviation σ_v.

ΔT [min]	h	$v_{\max}$ [m s^{-1}]	v_{mean} [m s^{-1}]
15	2	1.46	0.33 ± 0.20
15	5	1.04	0.23 ± 0.14
15	10	0.93	0.17 ± 0.12
15	15	0.79	0.14 ± 0.10
15	20	0.71	0.12 ± 0.09
30	2	1.10	0.26 ± 0.15
30	5	0.91	0.19 ± 0.12
30	10	0.77	0.15 ± 0.11
30	15	0.70	0.12 ± 0.09
30	20	0.62	0.11 ± 0.08
60	2	0.85	0.21 ± 0.13
60	5	0.78	0.16 ± 0.11
60	10	0.69	0.13 ± 0.09
60	15	0.60	0.11 ± 0.08
60	20	0.52	0.09 ± 0.07
90	2	0.75	0.19 ± 0.12
90	5	0.77	0.15 ± 0.10
90	10	0.66	0.12 ± 0.08

3.2.4 Noise Adaptive Fuzzy Equalization Method

The Noise Adaptive Fuzzy Equalization (NAFE, Druckmüller, 2013) method is a qualitative method for processing solar EUV images to improve their contrast. In the following the theory is presented as it is laid out in Druckmüller (2013).

There are, among others, two classical methods, which are combined in the NAFE method: convolution (e.g., Gonzalez and Woods, 2002) and adaptive histogram equalization (Pizer *et al.*, 1987). In the convolution or unsharp masking method the original image A is convolved with a kernel C to create the resulting image:

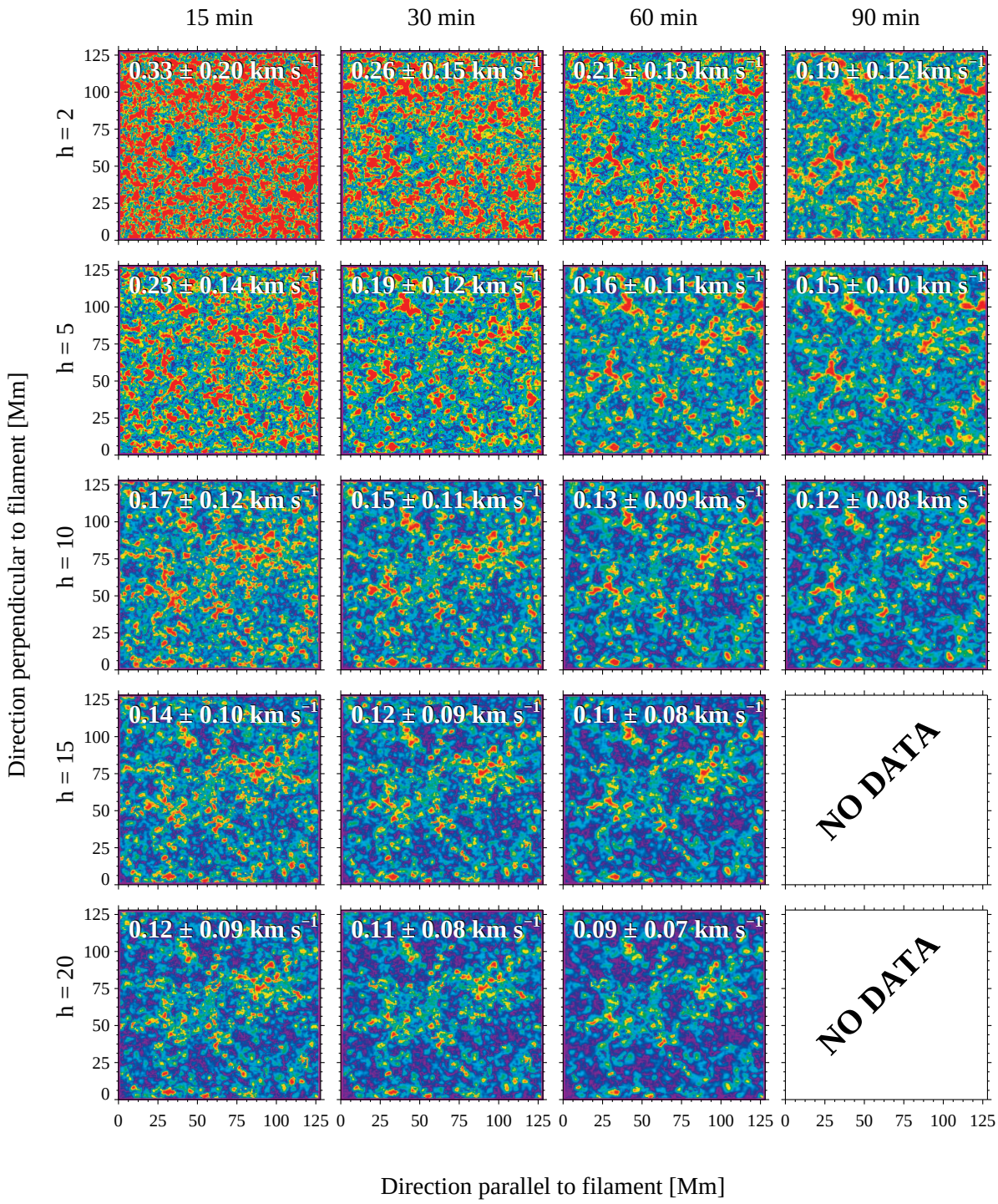

Figure 3.9: Flow speed map for different time intervals ΔT = 15, 30, 60, and 90 min and time cadences $\Delta t'$ given by different parameters h = 2, 5, 10, 15, and 20. At the top of each map, we mention the mean values of the velocity for this region with its standard deviation σ_v. Because of the chosen value for h = 15 and 20, averaging over the 90 min time interval is not possible. The color scale is the same as in Fig. 3.8. With constant h, the mean value of the velocity decreases with increasing time interval and with constant time interval ΔT, the mean and maximum velocities increases with decreasing h.

$$B = A \otimes C = A \otimes (D - L) = A - A \otimes L = A - M, \tag{3.21}$$

where D is a Dirac kernel with the property $A \otimes D = A$, and L denotes the kernel of a low-pass filter. The variable M is called unsharp mask. Normally the high-contrast features are in the low spatial-frequency

regime so that the resulting image B has a significantly lower dynamic range than image A. The AIA images have high-contrast features at high-spatial frequencies, for example, in bright loops. This is, why the convolution method is not very effective in enhancing AIA images.

Another classical technique for image processing is adaptive histogram equalization (Pizer *et al.*, 1987). The value of each pixel is transformed based on the histogram of the neighboring pixels. The method is very good for a high-dynamic range and can handle extreme contrast very well. Again some problems appear, as artifacts appear because of the morphology of the neighborhood. Thus, the surroundings influence the displayed coronal structures significantly. Another problem is that, because of the lower contrast, parts of the noise will be extremely amplified and faint details will be lost.

The NAFE method combines both classical methods, whereby it does not suffer from the typical problems encountered in these methods (Druckmüller, 2013). The resulting images are free of processing artifacts and the noise is well controlled and suppressed. The pixels of the original image A have a linear dependence on the intensity of coronal emission. The resulting image B is then a linear combination of the two images $T_\gamma(A)$ and $E_{N,\sigma}(A)$:

$$B = (1-w)T_\gamma(A) + wE_{N,\sigma}. \tag{3.22}$$

The image $T_\gamma(A)$ is a gamma transform of image A (see Eq. 3.23). The pixel are passed through a constant pixel value transform

$$y = b_0 + (b_0 + b_1)\left(\frac{x-a_0}{a_1-a_0}\right)^{\gamma^{-1}}, \tag{3.23}$$

where a_0 and a_1 are constant input values, representing the zero emission intensity and the maximum value encountered in the data. The constants b_0 and b_1 are the minimum and maximum output values. The standard value is $\gamma = 2.2$. Using lower values for γ yield darker images, and higher values make the images brighter. The image $T_\gamma(A)$ gives an "unmodified" image; the image $E_{N,\sigma}(A)$ is created by the NAFE method. Important for the NAFE method is the constant w, which represents the NAFE weight. Typical values for w are between 0.05 and 0.3. By choosing the value $w = 0$ the image pass only through the normal gamma transformation. The NAFE method transforms each pixel individually with respect to its neighborhood. In this method the idea is to assume a uniform brightness level distribution, where all pixel values of the resulting image have the same probability. The advantage of the adaptive histogram equalization is that the cumulative histogram is only computed for the processed neighborhood of the pixel. Often a square neighborhood is used in this method. Thereby, the results depend on the shape and the size of this neighborhood and contain several artifacts. The improvement in the NAFE method is to use a fuzzy neighborhood and not a constant. Analog to the convolution the process takes advantage of a non-constant neighborhood. A convolution with a constant kernel results in an inferior low-pass filter which has a complicated Fourier spectrum. By using a Gaussian kernel, better results can be obtained. Thus, in the NAFE method a fuzzy neighborhood $\tilde{L}^n_{i,j}(x)$ is used which leads to a fuzzy histogram $h^n_{i,j}(x)$, a normalized cumulative fuzzy histogram $C^n_{i,j}(x)$, and a fuzzy equalizing function

$$f^n_{i,j}(x) = b_0 + (b_1 - b_0)C^n_{i,j}(x). \tag{3.24}$$

Unlike Eq. 3.23 the function differs for every pixel $a_{i,j}$. The output pixels $q_{i,j}$ are defined as

$$q_{i,j} = f^n_{i,j}(a_{i,j}). \tag{3.25}$$

Most of the problems of the classical histogram equalization can be solved with this method. But the method has problems with extreme amplification of additive noise in areas with low contrast. In such regions faint low contrast details will be lost. Druckmüller (2013) solves this problem by adding artificial additive noise to the image, which is used for computing the histogram. Thereby the contrast of the original noise of the image will decrease. The cumulative fuzzy histogram is convolved with the noise distribution, i.e., a Gaussian distribution.

Druckmüller (2013) remarks that the NAFE method shows the best results for AIA 171 Å images. The images are artifact-free whereby contrast and noise are well controlled. The only disadvantage is the long processing time of the method.

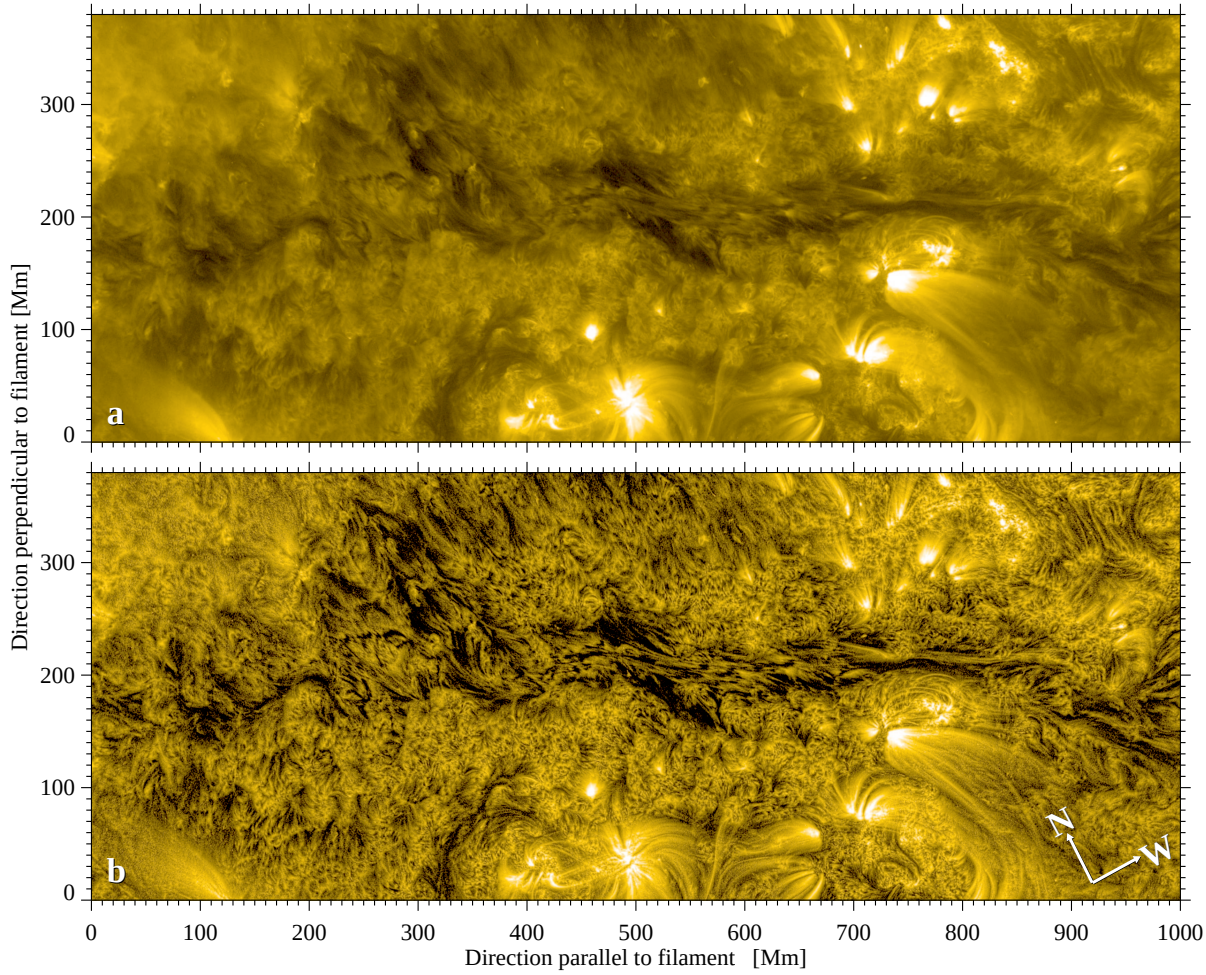

Figure 3.10: Comparison of (a) the unprocessed AIA 171 Å image with (b) the image processed with NAFE. The contrast is significantly improved in image (b), and the structure details are clearly visible, i.e., in the loops of the emerging flux region. The spine of the filament with its threads and the anti-parallel flows in the movies are easily recognized.

Processing the AIA 171 Å Images with NAFE

We apply the NAFE method to the AIA 171 Å images, and we get a much improved contrast of the image. We choose the following input parameters for the image processing: $a_0 = 40$ and $a_1 = 6256$. The values are the same for all images and are chosen based on the values of the first image. A γ-value = 2.6 and $w = 0.25$ for the NAFE parameter deliver visually the best results. The NAFE algorithm gives the following output values: $b_0 = 6904$ and $b_1 = 55041$. In Fig. 3.10 we compare the original image, which is processed as explained in Section 2.5.1, with the processed image by NAFE. It is evident that the NAFE image shows a higher contrast. The structures in the images are sharper and richer in detail. We can see single loops in the EFR and other active regions, and we uncover single threads in the filament's spine.

In movies of the time-series of the high-cadence data set, we even detect counter-streaming flows of plasma along the filament's spine (see region A in Fig. 3.11). Alexander *et al.* (2013) uncovered first the anti-parallel flows along filament threads in the EUV. The observations were made with the Highresolution Coronal Imager (Hi-C, Cirtain *et al.*, 2013), which has a better resolution of $0\farcs2$ than AIA with $1\farcs5$ (Lemen *et al.*, 2012). Alexander *et al.* (2013) study an active region filament in the 193 Å wavelength band both with Hi-C and AIA. They conclude that they cannot identify anti-parallel flows in AIA images without a priori knowledge of the sub-arcseconds observations of Hi-C. Even with image processing the observation of the anti-parallel flows in the AIA images is very difficult (Alexander *et al.*, 2013).

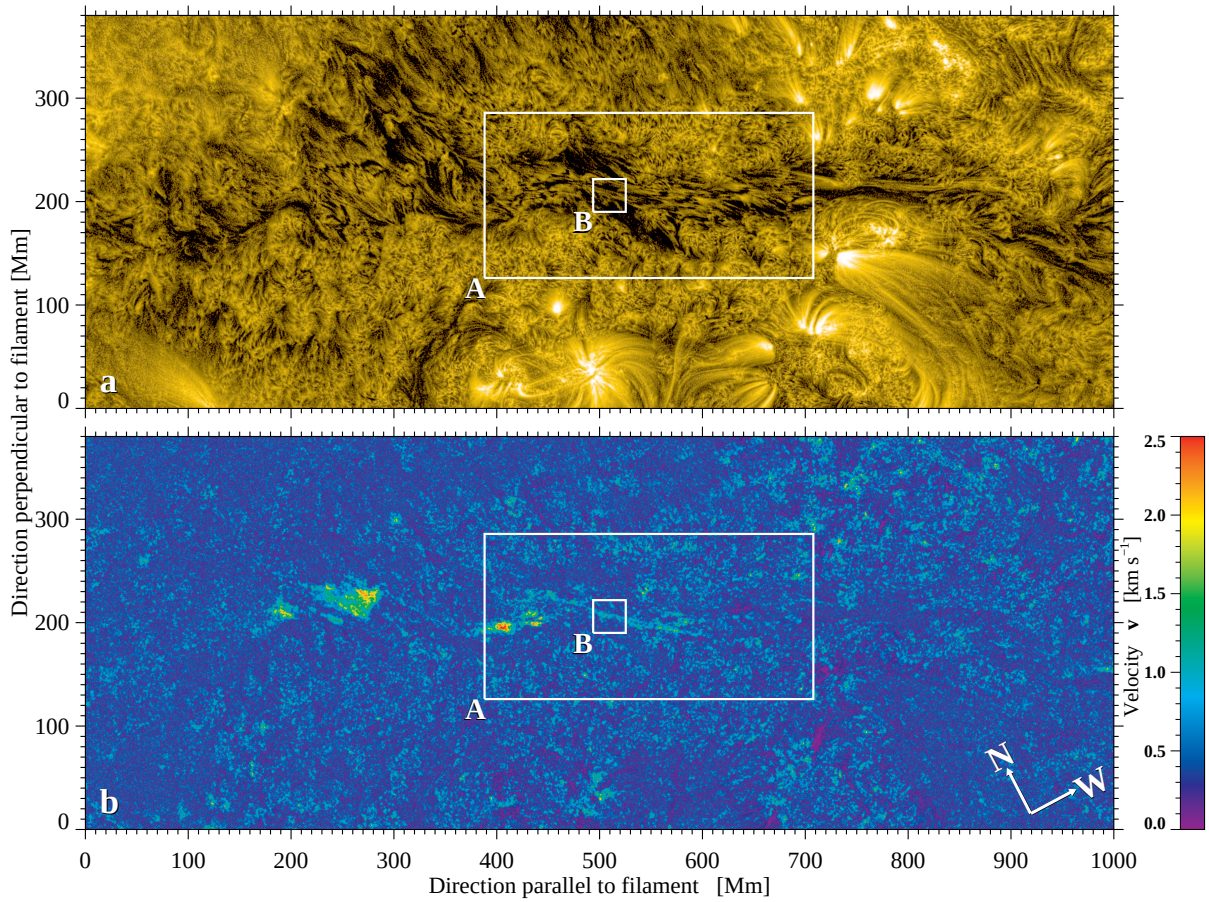

Figure 3.11: (a) Processed AIA 171 Å image of the reference map on 16 November 2011 at 12:00 UT and (b) LCT flow speed map based on AIA 171 Å images. We use region A to determine how flow fields depend on the averaged time interval. In region B we quantify the counter-streaming flows.

In our observations of the giant quiet-Sun filament and even in the unprocessed images anti-parallel flows are discernible, maybe because the filament threads are bigger. With NAFE it is possible to see the anti-parallel flows of plasma in the filament very clearly. Later, we use the LCT to quantify the counter-streaming flows and their velocities.

Velocity of the Lower Corona from AIA 171 Å Images with Local Correlation Tracking

The AIA 171 Å images show the lower corona of the Sun. In the high-cadence data set of ΔT = 120 min are 601 images with a time cadence of Δt = 12 s. In the LCT algorithm we use a time cadence of $\Delta t'$ = 8 · 12 s = 96 s. With LCT we get a mean velocity of v_{mean} = (0.42 ± 0.25) km s^{-1} and a maximum velocity of v_{max} = 3.35 km s^{-1}. Figure 3.11 shows the original image on 16 November 2011 at 12:00 UT already processed with NAFE and the flow speed map averaged over the 2-hour time interval. The red areas show clearly the parts with high velocity values. They trace the filament.

To inspect the LCT results more closely, we choose a ROI of 300 Mm×150 Mm within the AIA 171 Å images along the spine of the filament (see region A in Fig. 3.11). First, we study how the time interval ΔT impacts the velocity. Hence, we run the LCT algorithm for ΔT = 15, 30, 60, 90, and 120 min.

In Fig. 3.12 the results for the time intervals ΔT = 30, 60, 90, and 120 min are displayed. In Tab. 3.2 the maximum and mean values as well as the standard derivation σ_v for the velocities are listed. For the shorter time intervals the velocity values are higher. The highest results belong to the 15-minute time interval with a maximum velocity value of v_{max} = 7.73 km s^{-1}. The lowest maximum values v_{max} = 3.35 km s^{-1} are found for the 120-minute time interval. This tendency of getting higher velocity values matches that of the DAVE method in Section 3.2.3. In the 30-minute time interval small groups with high velocity values are present around the spine (see Fig. 3.12a). The longer the time interval, the smaller

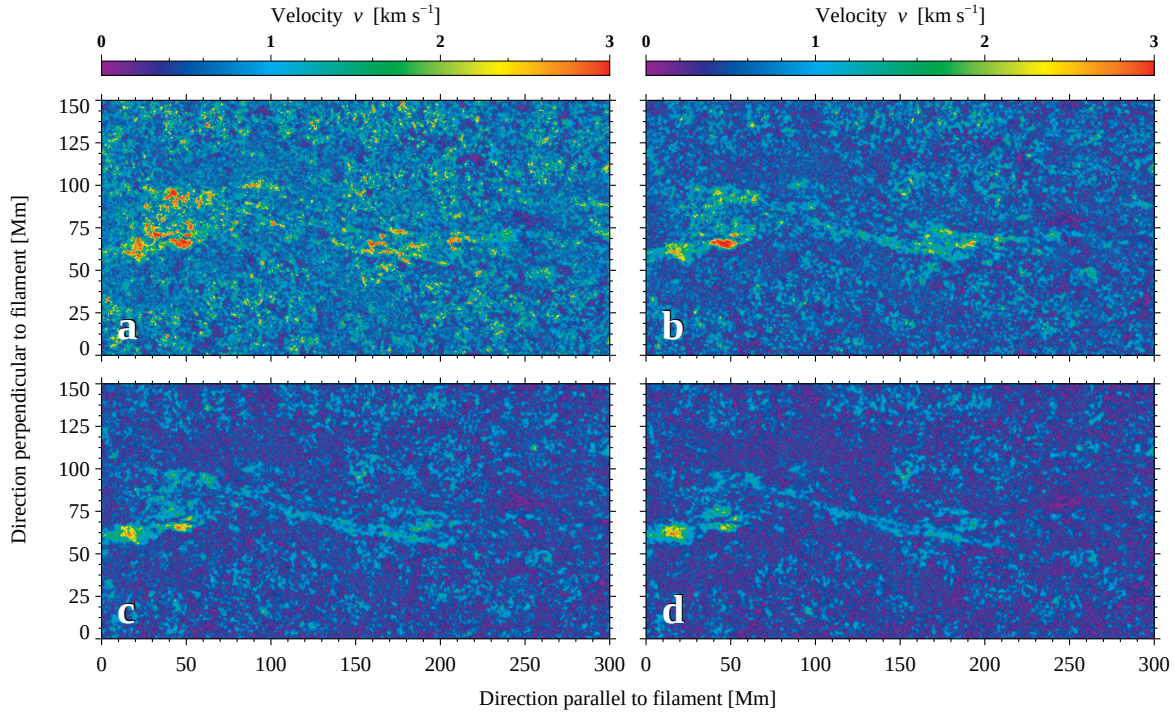

Figure 3.12: The LCT velocity maps for different time intevals ΔT for a region in the middle of the filament of 300 Mm×150 Mm. The time intervals are (a) ΔT = 30 min, (b) ΔT = 60 min, (c) ΔT = 90 min, and (d) ΔT = 120 min.

Table 3.2: Comparison of the mean and maximum velocities of the AIA 171 Å flow maps for different time intervals ΔT of the LCT algorithm for a region of 300×150 Mm. The longer the time interval, the smaller are the mean and maximum velocities.

ΔT [min]	v_{max} [km s^{-1}]	v_{mean} [km s^{-1}]
15	7.73	1.22 ± 0.76
30	6.19	0.85 ± 0.53
60	4.55	0.61 ± 0.38
90	3.27	0.51 ± 0.31
120	3.35	0.45 ± 0.28

are the regions. However, in the longer time intervals the overall flow along the spine becomes visible. More random velocity vectors average out and only persistent flows along the spine remain.

Determination of Counter-Streaming Flows with Local Correlation Tracking

We want to quantify the counter-streaming flows with the help of the LCT velocity results. Therefore, we display a smaller region of 100 Mm×100 Mm (see region B in Fig. 3.11) and the corresponding velocity vectors for the 15-minute time interval (see Fig. 3.13). In this FOV, these flows are initially detected in the movies. We see an up-streaming flow in the left part of the image and an down-streaming flow on the right side (see Fig. 3.13a). In Fig. 3.13b, we present an azimuth map. The direction of the flows is given by the 12-color compass rose in the upper right corner. The up-streaming flow is displayed in violet and the down-streaming flow in chartreuse green. The azimuth map was smoothed with a Lee (1986) filter to more clearly display the counter-streaming flows. In Fig. 3.14 we see the velocity for the 90-minute time interval. Still, the counter-streaming is recognizable. The velocities have smaller values than in the 15-minute time interval, because six times more velocity vectors are averaged. The up-streaming flow reaches higher velocities than the down-streaming one. There is also a larger region of divergent flows. Figure 3.14b shows the azimuth map for this region. Here, the up-streaming magenta flows and down-streaming green flows are showing the counter-streaming, too.

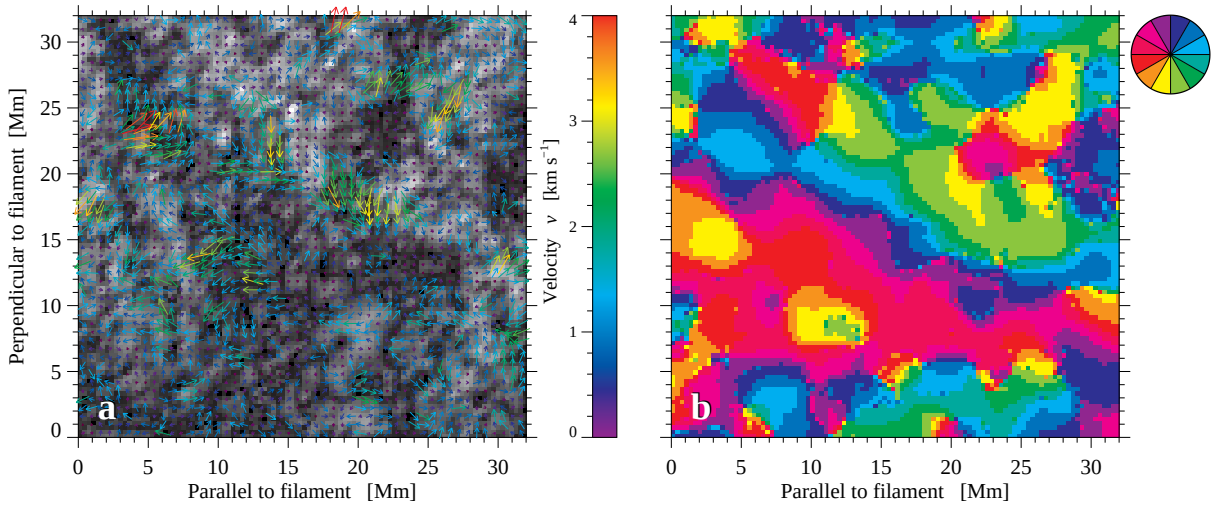

Figure 3.13: (a) Anti-parallel flows in a region of 100 Mm×100 Mm along the spine region of the filament for the 15-minute time-series. (b) Azimuth map of the velocities. The 12-color compass rose in the upper right corner denotes the direction of the streaming plasma.

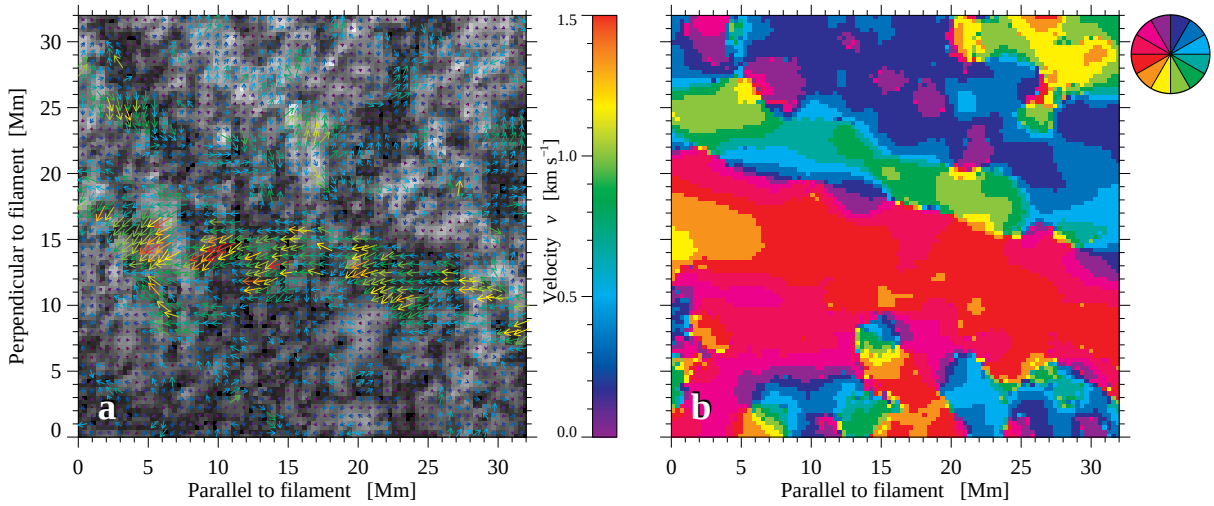

Figure 3.14: (a) Anti-parallel flows in a region of 100 Mm×100 Mm along the spine region of the filament for the 90-minute time-series. (b) Azimuth map of the velocities. Both maps show the counter-streaming flows.

3.3 Discussion

We measure the velocities for different layers of the solar atmosphere with two different methods, LCT and DAVE. We get the smallest velocities with the DAVE method with a mean velocity of v_{mean} = (0.08 $\pm$ 0.06) km s^{-1} (see Table 3.3). The mean velocities for LCT reach higher values. For HMI continuum images we obtain mean velocities of v_{mean} = (0.44 $\pm$ 0.24) km s^{-1} and for AIA 171 Å images v_{mean} = (0.42 $\pm$ 0.25) km s^{-1}. We achieve the highest values for the AIA 1600 Å images with a mean velocity of v_{mean} = (0.84 $\pm$ 0.51) km s^{-1}.

LCT tracks on contrast structures, which is in the case of the quiet-Sun photosphere the isotropic pattern of the granulation. Persistent flows are related to plasma motions resulting in the well-known flow patterns for meso- and supergranulation (November and Simon, 1988). In the vicinity of sunspots we encounter the moat flow, and also penumbral filaments and umbral dots provide sufficient contrast to be tracked. DAVE, however, tracks the evolution of the magnetic fields itself, i.e., in the quiet Sun it measures the motions of small-scale flux bundles being jostled around by the granular motions. Consequently, it takes a longer time to measure the persistent flux transport velocities in the quiet Sun. The

Table 3.3: Comparison of velocity measurements with DAVE and LCT methods for different atmospheric layers.

Image	Method	v_{mean} [km s^{-1}]	v_{max} [km s^{-1}]
Magnetogram	DAVE	0.08 ± 0.06	0.89
Continuum Image	LCT	0.44 ± 0.24	3.21
1600 Å Image	LCT	0.84 ± 0.51	4.90
171 Å Image	LCT	0.42 ± 0.25	3.35

moat flow, which is associated with sunspots, has significantly higher flux transport velocities than the quiet Sun. Finally, LCT applied to the AIA 1600 Å images is confronted with the highly dynamic chromospheric brightenings, which not only move but also blink in and out of existence in place. Thus, longer time averages are needed to reliably track persistent flows. Flows near concentrations of magnetic flux are diminished in the quiet Sun, because these flux concentrations typically reside quasi-stationary in the chromospheric network or in the vertices of supergranular boundaries.

We show that the velocity in shorter time intervals is higher than in longer ones. For the AIA 171 Å images we study the velocities in the spine region for different time intervals and obtain differences of the maximum velocity value of 40% between the smallest (15 min) and the biggest time interval. In the 15-minute time interval the velocities reach values up to 7.73 km s^{-1}.

Alexander *et al.* (2013) measured the velocity in the AIA 193 Å wavelength band for active region filaments and got results of $v_{\mathrm{mean}} = (84 \pm 15)$ km s^{-1}. Both the AIA 193 Å and 171 Å wavelength band measurements provide horizontal flow speeds in the corona, where active region filaments reach much higher velocities than quiet-Sun filaments. Zirker, Engvold, and Yi (1994) measured velocities of quiet-Sun prominences in Hα. They obtained mean velocities of $v_{\mathrm{mean}} = 3$–5 km s^{-1} and maximum velocities $v_{\mathrm{max}} = 20$ km s^{-1}. They use feature tracking to determine the velocities. Our velocities are smaller than the results of Zirker, Engvold, and Yi (1994), but this can be explained by our choice of the LCT and DAVE methods. We can assume that our velocities give a lower estimate of the velocities, because we average over a certain time interval to measure persistent flow and not the proper motions of individual features.

One important result is the observation of the counter-streaming flows along the filament's spine. Alexander *et al.* (2013) did not detect these flows in AIA images, maybe because they observed a much smaller active region filament. The NAFE-processed data show very clearly the counter-streaming flows along the spine. We discovered the counter-streaming flows in the velocity maps computed with the LCT algorithm. In future work, we want to use a variety of other methods to quantify the counter-streaming flows.

Chapter 4

Conclusions

When you have eliminated
all which is impossible,
then whatever remains,
however improbable,
must be the truth.

Doyle (1890)

In this work, we analyzed the evolution and the dynamics of a giant solar filament. Kuckein, Denker, and Verma (2014) observed the filament in Hα with the VTT on Tenerife. It is a quiet-Sun filament stretching from high latitudes to the activity belt. To see the whole development of the filament, we decided to use SDO data and get more detailed information about the dynamics of and the processes within the filament. The various data of SDO instruments AIA and HMI allow us to see the filament in different layers of the solar atmosphere from the photosphere, via the chromosphere, up into the corona. Therefore, we utilized two different data sets: a long-duration data set with data from two weeks between 8–22 November 2011 and a high-cadence data set with data of two hours on 16 November 2011 from 11:00–13:00 UT, when the filament crossed the central meridian of the Sun. The long-duration data set contains 336 images for each AIA wavelength band and HMI filtergram concerning the time cadence of one hour. We used the AIA wavelength bands 171 Å, 191 Å, 211 Å, 304 Å, and 1600 Å and the HMI continuum images and magnetograms. In the high-cadence data set, we used the same images but with a different time cadence. The AIA wavelength bands of 171 Å, 191 Å, 211 Å, and 304 Å have a time cadence of 12 s, the AIA 1600 Å wavelength band has a time cadence of 24 s, and the HMI filtergrams and magnetograms have a time cadence of 45 s. Thus, the data sets contain either 600, 300, or 160 images depending the different time cadences.

First of all, we processed each image (Chapter 2). For this purpose, we used IDL routines to perform corrections of the limb darkening, differential rotation, and geometric foreshortening. The programs work with a minimum of user interaction.

By inspecting the long-duration data set, we scrutinized the evolution of the filament (Chapter 3). In the photosphere, we determined the development of the magnetic field and the appearance of sunspots, as seen in the continuum images. The filament plasma lies in the chromosphere and the corona, where we can see the rapid evolution of the filament by releasing two major eruptions. Both eruptions caused CMEs which were not geo-effective.

The main work of this thesis was to analyze the dynamics of the filament (Chapter 3). We applied two existing methods for determining the velocity of the magnetic field structure and the filament plasma in photosphere, chromosphere, and corona. Before implementing the LCT algorithm and applying it to the coronal data we process the images to obtain a better contrast. For this purpose, we use the new method NAFE, which gives very good results, i.e., the detail-rich images with a high dynamic range. Thanks to this method it was even possible to uncover counter-streaming flows along the filament's spine.

The algorithms for the determination of the velocities delivered different results for the velocities. The DAVE algorithm, which measures the magnetic proper motions within consecutive magnetograms, gave us the smallest velocities for the whole filament of $v_{\mathrm{DAVE,mean}} = (0.08 \pm 0.06)$ km s^{-1}. The velocities derived with LCT were higher. For the photosphere, we obtained a higher mean velocity $v_{\mathrm{LCT,mean}} = (0.44 \pm 0.24)$ km s^{-1}, and for the corona we achieved a mean velocity $v_{\mathrm{LCT,mean}} = (0.42 \pm 0.25)$ km s^{-1}. The highest mean velocity we got in the chromosphere for the AIA 1600 Å wavelength band with $v_{\mathrm{LCT,mean}} = (0.84 \pm 0.51)$ km s^{-1}. LCT tracks in the photosphere the isotropic patterns of the granulation. However, DAVE tracks the evolution of the magnetic field itself. Because of the brightenings in the chromosphere, the AIA 1600 Å images had to be averaged over a longer time interval to get reliable flow velocities.

For the magnetic structure, we looked more closely at the EFR, which appeared between the 14–19 November 2011. There, we varied the time interval and the time cadence and found a dependence on both parameters. A closer look at this region also revealed divergent and convergent flows around the sunspots in this region. As for DAVE, we changed the time interval for LCT, but for a region around the filament's spine and carried out a parameter study. We obtained the same results, i.e., the velocity becomes smaller by increasing the time interval.

The most astonishing results was the discovery of counter-streaming flows in AIA 171 Å images. It was even possible to quantify the anti-parallel flows with the LCT algorithm, both for the 15-minute as for the 90-minute time interval.

But still further work can be done by studying the counter-streaming. We plan to use other methods, e.g., cork maps where flows can be visualized by following a virtual tracer particle in the streaming plasma. We plan also to vary the size of the kernel or the FWHM. We assume that the counter-streaming flows are better visible with a smaller kernel.

The great amount of data from the SDO gave me the opportunity to perform a in-depths study of quiet-Sun filaments and learn much more about the solar-terrestrial relations.

During the Bachelor thesis, I learned much about the physical processes on the Sun. The thesis gave me the opportunity to compare the different layers of the Sun and see the full evolution of a giant solar filament. Such filaments are very rare objects on the Sun and I am glad that I got the chance to analyze this structure learning so much about the Sun's dynamics. I hope to continue the work about filaments and other solar features in the context of a Master thesis and also a PhD thesis. Maybe it will be possible not only to use the remote observations of SDO, but also to carry out observations by myself.

Bibliography

Alexander, C.E., Walsh, R.W., Régnier, S., Cirtain, J., Winebarger, A.R., Golub, L., Kobayashi, K., Platt, S., Mitchell, N., Korreck, K., DePontieu, B., DeForest, C., Weber, M., Title, A., Kuzin, S.: 2013, Anti-Parallel EUV Flows Observed along Active Region Filament Threads with Hi-C. *Astrophys. J., Lett.* **775**, L32 – L37, doi:10.1088/2041-8205/775/1/L32.

Anzer, U., Heinzel, P.: 2005, On the Nature of Dark Extreme Ultraviolet Structures Seen by SOHO/EIT and TRACE. *Astrophys. J.* **622**, 714 – 721, doi:10.1086/427817.

Balthasar, H., Beck, C., Louis, R.E., Verma, M., Denker, C.: 2014, Near-Infrared Spectropolarimetry of a δ-Spot. *Astron. Astrophys.* **562**, L6 – L9, doi:10.1051/0004-6361/201323224.

Bentely, R.D., Freeland, S.L.: 1998, SOLARSOFT – An Analysis Environment for Solar Physics. In: *Crossroads for European Solar and Heliospheric Physics. Recent Achievements and Future Mission Possibilities, ESA Special Publication* **417**, 225 – 228.

Berghmans, D., Hochedez, J.F., Defise, J.M., Lecat, J.H., Nicula, B., Slemzin, V., Lawrence, G., Katsyiannis, A.C., van der Linden, R., Zhukov, A., Clette, F., Rochus, P., Mazy, E., Thibert, T., Nicolosi, P., Pelizzo, M.G., Schühle, U.: 2006, SWAP Onboard PROBA 2, a New EUV Imager for Solar Monitoring. *Adv. Space Res.* **38**, 1807 – 1811, doi:10.1016/j.asr.2005.03.070.

Boerner, P., Edwards, C., Lemen, J., Rausch, A., Schrijver, C., Shine, R., Shing, L., Stern, R., Tarbell, T., Title, A., Wolfson, C.J., Soufli, R., Spiller, E., Gullikson, E., McKenzie, D., Windt, D., Golub, L., Podgorski, W., Testa, P., Weber, M.: 2012, Initial Calibration of the Atmospheric Imaging Assembly (AIA) on the Solar Dynamics Observatory (SDO). *Sol. Phys.* **275**, 41 – 66, doi:10.1007/s11207-011-9804-8.

Brown, D., Regnier, S., Marsh, M., Bewsher, D.: 2011, Working with Data from the Solar Dynamics Observatory. Technical Report, University of Central Lancashire. Version 1.2.

Cartledge, N.P., Titov, V.S., Priest, E.R.: 1996, A 2-D Model for the Support of a Polar-Crown Solar Prominence. *Sol. Phys.* **166**, 287 – 310, doi:10.1007/BF00149400.

Chae, J., Sakurai, T.: 2008, A Test of Three Optical Flow Techniques – LCT, DAVE, and NAVE. *Astrophys. J.* **689**, 593 – 612, doi:10.1086/592761.

Cirtain, J.W., Golub, L., Winebarger, A.R., de Pontieu, B., Kobayashi, K., Moore, R.L., Walsh, R.W., Korreck, K.E., Weber, M., McCauley, P., Title, A., Kuzin, S., Deforest, C.E.: 2013, Energy Release in the Solar Corona from Spatially Resolved Magnetic Braids. *Nature* **493**, 501 – 503, doi:10.1038/nature11772.

Delaboudinière, J.P., Artzner, G.E., Brunaud, J., Gabriel, A.H., Hochedez, J.F., Millier, F., Song, X.Y., Au, B., Dere, K.P., Howard, R.A., Kreplin, R., Michels, D.J., Moses, J.D., Defise, J.M., Jamar, C., Rochus, P., Chauvineau, J.P., Marioge, J.P., Catura, R.C., Lemen, J.R., Shing, L., Stern, R.A., Gurman, J.B., Neupert, W.M., Maucherat, A., Clette, F., Cugnon, P., van Dessel, E.L.: 1995, EIT: Extreme-Ultraviolet Imaging Telescope for the SOHO Mission. *Sol. Phys.* **162**, 291 – 312, doi:10.1007/BF00733432.

Dere, K.P., Landi, E., Mason, H.E., Monsignori Fossi, B.C., Young, P.R.: 1997, CHIANTI – An Atomic Database for Emission Lines. *Astron. Astrophys. Suppl. Ser.* **125**, 149 – 173, doi:10.1051/aas:1997368.

DeRosa, M., Slater, G.: 2013, *Guide to SDO DATA Analysis*. Lockheed Martin Solar & Astrophysics Laboratory, Palo Alto, California.

Domingo, V., Fleck, B., Poland, A.I.: 1995, The SOHO Mission: An Overview. *Sol. Phys.* **162**, 1 – 37, doi:10.1007/BF00733425.

Doyle, A.C.: 1890, *The Sign of the Four*, Spencer Blackett, London, UK.

Druckmüller, M.: 2013, A Noise Adaptive Fuzzy Equalization Method for Processing Solar Extreme Ultraviolet Images. *Astrophys. J., Suppl. Ser.* **207**, 25 – 29, doi:10.1088/0067-0049/207/2/25.

Eddy, J.A.: 1974, A Nineteenth-Century Coronal Transient. *Astron. Astrophys.* **34**, 235 – 240.

Engvold, O.: 1998, Observations of Filament Structure and Dynamics. In: Webb, D.F., Schmieder, B., Rust, D.M. (eds.) *New Perspectives on Solar Prominences*, *ASP Conf. Ser.* **150**, 23 – 31.

Freeland, S.L., Handy, B.N.: 1998, Data Analysis with the SolarSoft System. *Sol. Phys.* **182**, 497 – 500, doi:10.1023/A:1005038224881.

Gaizauskas, V., Zirker, J.B., Sweetland, C., Kovacs, A.: 1997, Formation of a Solar Filament Channel. *Astrophys. J.* **479**, 448 – 457, doi:10.1086/512788.

Gonzalez, R.C., Woods, R.E.: 2002, *Digital Image Processing*, Prentice-Hall, Upper Saddle River, New Jersey.

Handy, B.N., Acton, L.W., Kankelborg, C.C., Wolfson, C.J., Akin, D.J., Bruner, M.E., Caravalho, R., Catura, R.C., Chevalier, R., Duncan, D.W., Edwards, C.G., Feinstein, C.N., Freeland, S.L., Friedlaender, F.M., Hoffmann, C.H., Hurlburt, N.E., Jurcevich, B.K., Katz, N.L., Kelly, G.A., Lemen, J.R., Levay, M., Lindgren, R.W., Mathur, D.P., Meyer, S.B., Morrison, S.J., Morrison, M.D., Nightingale, R.W., Pope, T.P., Rehse, R.A., Schrijver, C.J., Shine, R.A., Shing, L., Strong, K.T., Tarbell, T.D., Title, A.M., Torgerson, D.D., Golub, L., Bookbinder, J.A., Caldwell, D., Cheimets, P.N., Davis, W.N., Deluca, E.E., McMullen, R.A., Warren, H.P., Amato, D., Fisher, R., Maldonado, H., Parkinson, C.: 1999, The Transition Region and Coronal Explorer. *Sol. Phys.* **187**, 229 – 260, doi:10.1023/A:1005166902804.

Hanisch, R.J., Farris, A., Greisen, E.W., Pence, W.D., Schlesinger, B.M., Teuben, P.J., Thompson, R.W., Warnock, A.: 2001, Definition of the Flexible Image Transport System (FITS). *Astron. Astrophys.* **376**, 359 – 380, doi:10.1051/0004-6361:20010923.

Hirayama, T.: 1985, Modern Observations of Solar Prominences. *Sol. Phys.* **100**, 415 – 434, doi:10.1007/BF00158439.

Howard, R.A., Moses, J.D., Vourlidas, A., Newmark, J.S., Socker, D.G., Plunkett, S.P., Korendyke, C.M., Cook, J.W., Hurley, A., Davila, J.M., Thompson, W.T., St Cyr, O.C., Mentzell, E., Mehalick, K., Lemen, J.R., Wuelser, J.P., Duncan, D.W., Tarbell, T.D., Wolfson, C.J., Moore, A., Harrison, R.A., Waltham, N.R., Lang, J., Davis, C.J., Eyles, C.J., Mapson-Menard, H., Simnett, G.M., Halain, J.P., Defise, J.M., Mazy, E., Rochus, P., Mercier, R., Ravet, M.F., Delmotte, F., Auchere, F., Delaboudiniere, J.P., Bothmer, V., Deutsch, W., Wang, D., Rich, N., Cooper, S., Stephens, V., Maahs, G., Baugh, R., McMullin, D., Carter, T.: 2008, Sun Earth Connection Coronal and Heliospheric Investigation (SECCHI). *Space Sci. Rev.* **136**, 67 – 115, doi:10.1007/s11214-008-9341-4.

Kaiser, M.L., Kucera, T.A., Davila, J.M., St Cyr, O.C., Guhathakurta, M., Christian, E.: 2008, The STEREO Mission: An Introduction. *Space Sci. Rev.* **136**, 5 – 16, doi:10.1007/s11214-007-9277-0.

Kosugi, T., Matsuzaki, K., Sakao, T., Shimizu, T., Sone, Y., Tachikawa, S., Hashimoto, T., Minesugi, K., Ohnishi, A., Yamada, T., Tsuneta, S., Hara, H., Ichimoto, K., Suematsu, Y., Shimojo, M., Watanabe, T., Shimada, S., Davis, J.M., Hill, L.D., Owens, J.K., Title, A.M., Culhane, J.L., Harra, L.K., Doschek, G.A., Golub, L.: 2007, The Hinode (Solar-B) Mission: An Overview. *Sol. Phys.* **243**, 3 – 17, doi:10.1007/s11207-007-9014-6.

Kuckein, C., Denker, C., Verma, M.: 2014, High-Resolution Spectroscopy of a Giant Solar Filament. In: Schmieder, B., Malherbe, J.M., Wu, S.T. (eds.) *Nature of Prominences and their Role in Space Weather*, *IAU Symp.* **300**, 437 – 438, doi:10.1017/S1743921313011447.

Kuckein, C., Centeno, R., Martínez Pillet, V., Casini, R., Manso Sainz, R., Shimizu, T.: 2009, Magnetic Field Strength of Active Region Filaments. *Astron. Astrophys.* **501**, 1113 – 1121, doi:10.1051/0004-6361/200911800.

Lang, K.R.: 2001, *The Cambridge Encyclopedia of the Sun*, Cambridge University Press, Cambridge, UK.

Lee, D.T., Schachter, B.J.: 1980, Two Algorithms for Constructing a Delaunay Triangulation. *Int. J. Comp. Info. Sci.* **9**, 219 – 242, doi:10.1007/BF00977785.

Lee, J.S.: 1986, Speckle Suppression and Analysis for Synthetic Aperture Radar Images. *Opt. Eng* **25**, 255636.

Leese, J.A., Novak, C.S., Clark, B.B.: 1971, An Automated Technique for Obtaining Cloud Motion from Geosynchronous Satellite Data Using Cross Correlation. *J. Appl. Meteorol.* **10**, 118 – 132.

Lemen, J.R., Title, A.M., Akin, P.F. D. J.and Boerner, Chou, C., Drake, J.F., Duncan, D.W., Edwards, C.G., Friedlaender, F.M., Heyman, G.F., Hurlburt, N.E., Katz, N.L., Kushner, G.D., Levay, M., Lindgren, R.W., Mathur, D.P., McFeaters, E.L., Mitchell, S., Rehse, R.A., Schrijver, C.J., Springer, L.A., Stern, R.A., Tarbell, T.D., Wuelser, J.P., Wolfson, C.J., Yanari, C., Bookbinder, J.A., Cheimets, P.N., Caldwell, D., Deluca, E.E., Gates, R., Golub, L., Park, S., Podgorski, W.A., Bush, R.I., Scherrer, P.H., Gummin, M.A., Smith, P., Auker, G., Jerram, P., Pool, P., Soufli, R., Windt, D.L., Beardsley, S., Clapp, M., Lang, J., Waltham, N.: 2012, The Atmospheric Imaging Assembly (AIA) on the Solar Dynamics Observatory (SDO). *Sol. Phys.* **275**, 17 – 40, doi:10.1007/s11207-011-9776-8.

Leroy, J.L., Bommier, V., Sahal-Brechot, S.: 1983, The Magnetic Field in the Prominences of the Polar Crown. *Sol. Phys.* **83**, 135 – 142, doi:10.1007/BF00148248.

Mackay, D.H., Karpen, J.T., Ballester, J.L., Schmieder, B., Aulanier, G.: 2010, Physics of Solar Prominences. II. Magnetic Structure and Dynamics. *Space Sci. Rev.* **151**, 333 – 399, doi:10.1007/s11214-010-9628-0.

Martin, S.F.: 1998a, Conditions for the Formation and Maintenance of Filaments. *Sol. Phys.* **182**, 107 – 137, doi:10.1023/A:1005026814076.

Martin, S.F.: 1998b, Filament Chirality: A Link Between Fine-Scale and Global Patterns. In: Webb, D.F., Schmieder, B., Rust, D.M. (eds.) *New Perspectives on Solar Prominences*, *ASP Conf. Ser.* **150**, 419 – 429.

Moldwin, M.: 2008, *An Introduction to Space Weather*, Cambridge University Press, New York, USA.

November, L.J., Simon, G.W.: 1988, Precise Proper-Motion Measurement of Solar Granulation. *Astrophys. J.* **333**, 427 – 442, doi:10.1086/166758.

Panesar, N.K., Innes, D.E., Schmit, D.J., Tiwari, S.K.: 2014, On the Structure and Evolution of a Polar Crown Prominence/Filament System. *ArXiv e-prints: 1402.4989*.

Pardon, L., Worden, S.P., Schneeberger, T.J.: 1979, The Lifetimes of Sunspot Moats. *Sol. Phys.* **63**, 247 – 250, doi:10.1007/BF00174530.

Pereira, T.M.D., De Pontieu, B., Carlsson, M.: 2012, Quantifying Spicules. *Astrophys. J.* **759**, 18 – 33, doi:10.1088/0004-637X/759/1/18.

Pesnell, W.D., Thompson, B.J., Chamberlin, P.C.: 2012, The Solar Dynamics Observatory (SDO). *Sol. Phys.* **275**, 3 – 15, doi:10.1007/s11207-011-9841-3.

Pizer, S.M., Amburn, E.P., Austin, J.D., Cromartie, R., Geselowitz, A., Greer, T., ter Haar Romeny, B., Zimmerman, J.B., Zuiderveld, K.: 1987, Adaptive Histogram Equalization and its Variations. *Computer Vision, Graphics, and Image Processing* **39**, 355 – 368, doi:http://dx.doi.org/10.1016/S0734-189X(87)80186-X.

Raftery, C.L., Bloomfield, D.S., Gallagher, P.T., Seaton, D.B., Berghmans, D., De Groof, A.: 2013, Temperature Response of the 171 Å Passband of the SWAP Imager on PROBA2, with a Comparison to TRACE, SOHO, STEREO, and SDO. *Sol. Phys.* **286**, 111 – 124, doi:10.1007/s11207-013-0266-z.

Rice, R., Plaunt, J.: 1971, Adaptive Variable-Length Coding for Efficient Compression of Spacecraft Television Data. *Commun. Tech.* **19**, 889 – 897, doi:10.1109/TCOM.1971.1090789.

Santandrea, S., Gantois, K., Strauch, K., Teston, F., Tilmans, E., Baijot, C., Gerrits, D., De Groof, A., Schwehm, G., Zender, J.: 2013, PROBA2: Mission and Spacecraft Overview. *Sol. Phys.* **286**, 5 – 19, doi:10.1007/s11207-013-0289-5.

Scharr, H.: 2007, Optimal Filters for Extended Optical Flow. In: Jähne, B., Mester, R., Barth, B., Scharr, H. (eds.) *Complex Motion Lecture Notes in Computer Sciences* **3417**, Springer, Berlin, 14 – 29, doi:10.1007/978-540-69866-1_2.

Scherrer, P.H., Bogart, R.S., Bush, R.I., Hoeksema, J.T., Kosovichev, A.G., Schou, J., Rosenberg, W., Springer, L., Tarbell, T.D., Title, A., Wolfson, C.J., Zayer, I., MDI Engineering Team: 1995, The Solar Oscillations Investigation – Michelson Doppler Imager. *Sol. Phys.* **162**, 129 – 188, doi:10.1007/BF00733429.

Scherrer, P.H., Schou, J., Bush, R.I., Kosovichev, A.G., Bogart, R.S., Hoeksema, J.T., Liu, Y., Duvall, T.L., Zhao, J., Title, A.M., Schrijver, C.J., Tarbell, T.D., Tomczyk, S.: 2012, The Helioseismic and Magnetic Imager (HMI) Investigation for the Solar Dynamics Observatory (SDO). *Sol. Phys.* **275**, 207 – 227, doi:10.1007/s11207-011-9834-2.

Schou, J., Scherrer, P.H., Bush, R.I., Wachter, R., Couvidat, S., Rabello-Soares, M.C., Bogart, R.S., Hoeksema, J.T., Liu, Y., Duvall, T.L., Akin, D.J., Allard, B.A., Miles, J.W., Rairden, R., Shine, R.A., Tarbell, T.D., Title, A.M., Wolfson, C.J., Elmore, D.F., Norton, A.A., Tomczyk, S.: 2012, Design and Ground Calibration of the Helioseismic and Magnetic Imager (HMI) Instrument on the Solar Dynamics Observatory (SDO). *Sol. Phys.* **275**, 229 – 259, doi:10.1007/s11207-011-9842-2.

Schrijver, C.J., Zwaan, C.: 2008, *Solar and Stellar Magnetic Activity*, Cambridge University Press, Cambridge, UK.

Schuck, P.W.: 2005, Local Correlation Tracking and the Magnetic Induction Equation. *Astrophys. J., Lett.* **632**, L53 – L56, doi:10.1086/497633.

Schuck, P.W.: 2006, Tracking Magnetic Footpoints with the Magnetic Induction Equation. *Astrophys. J.* **646**, 1358 – 1391, doi:10.1086/505015.

Spitzer, L.: 1961, Flying Telescopes. *Bull. Atom. Sci.* **17**, 191 – 194.

Strous, L.H.: 1995, Feature Tracking: Deriving Horizontal Motion and More. In: *Helioseismology*, *ESA Special Publication* **376**, 213 – 217.

Thornton, L.M., Parnell, C.E.: 2011, Small-Scale Flux Emergence Observed Using Hinode/SOT. *Sol. Phys.* **269**, 13 – 40, doi:10.1007/s11207-010-9656-7.

van Ballegooijen, A.A., Martens, P.C.H.: 1989, Formation and Eruption of Solar Prominences. *Astrophys. J.* **343**, 971 – 984, doi:10.1086/167766.

Verma, M.: 2013, The Evolution and Decay of Sunspots – A High-Resolution Study of Flows and Magnetic Fields in and around Sunspots. PhD Thesis, Universität Potsdam.

Verma, M., Denker, C.: 2011, Horizontal Flow Fields Observed in Hinode G-Band Images. I. Methods. *Astron. Astrophys.* **529**, A153, doi:10.1051/0004-6361/201016358.

von der Lühe, O.: 1998, High-Resolution Observations with the German Vacuum Tower Telescope on Tenerife. *New Astron. Rev.* **42**, 493 – 497, doi:10.1016/S1387-6473(98)00060-8.

Vyssotsky, A.N.: 1949, *Astronomical Records in the Russian Chronicles from 1000 to 1600 AD (as Collected by D. O. Sviatsky*, Observatory Lund, Sweden.

Wells, D.C., Greisen, E.W., Harten, R.H.: 1981, FITS – A Flexible Image Transport System. *Astron. Astrophys. Suppl. Ser.* **44**, 363 – 370.

Woods, T.N., Eparvier, F.G., Hock, R., Jones, A.R., Woodraska, D., Judge, D., Didkovsky, L., Lean, J., Mariska, J., Warren, H., McMullin, D., Chamberlin, P., Berthiaume, G., Bailey, S., Fuller-Rowell, T., Sojka, J., Tobiska, W.K., Viereck, R.: 2012, Extreme Ultraviolet Variability Experiment (EVE) on the Solar Dynamics Observatory (SDO): Overview of Science Objectives, Instrument Design, Data Products, and Model Developments. *Sol. Phys.* **275**, 115 – 143, doi:10.1007/s11207-009-9487-6.

Zirker, J.B., Engvold, O., Martin, S.F.: 1998, Counter-Streaming Gas Flows in Solar Prominences as Evidence for Vertical Magnetic Fields. *Nature* **396**, 440 – 441, doi:10.1038/24798.

Zirker, J.B., Engvold, O., Yi, Z.: 1994, Flows in Quiescent Prominences. *Sol. Phys.* **150**, 81 – 86, doi:10.1007/BF00712878.

Zirker, J.B., Martin, S.F., Harvey, K., Gaizauskas, V.: 1997, Global Magnetic Patterns of Chirality. *Sol. Phys.* **175**, 27 – 44, doi:10.1023/A:1004946303735.

Acknowledgments

I would like to express my special appreciation and thanks to my supervisor Prof. Dr. Carsten Denker. Without his support and friendly comments this thesis would not be the same. It was a pleasure to work under his supervision, and I hope to continue the work for many years. Furthermore, I want to thank my co-advisor Prof. Dr. Gottfried Mann.

A special thanks to all the members of the Optical Solar Physics group at AIP. It is a pleasure to work with you. In particular, I would like to thank Drs. Horst Balthasar and Christoph Kuckein for proof-reading my thesis. Many thanks for the comments and suggestions you have made. I would like to thank also Sergio J. González Manrique for proof-reading the formulas in this thesis and Dr. Meetu Verma for her support and encouragement.

A great thanks to all my friends, who supported me during the bachelor thesis, in particular to Stuff, Ulli, Vicky, Phili, and Daniel for carefully reading the work. Furthermore, I want to thank my parents for their support and the encouragement I get from them. Especially I am grateful for the feedback of my sister Michaela and the support of her family. Above all I want to thank my boyfriend Marco, who was always there for me and listened to me.

The Solar Dynamics Observatory is developed and launched by NASA. The SDO data are provided by the Joint Science Operations Center – Science Data Processing at Stanford University. This research has made use of NASA's Astrophysics Data System. SolarSoftWare is a public-domain software package for analysis of solar data written in the Interactive Data Language by Exelis Visual Information Solutions. Only thanks to the free and easy access of data and programs, a fast analysis was possible in the short time period allotted to a Bachelor thesis.

Appendix A – List of Acronyms

AIA	Atmospheric Imaging Assembly
AIP	Leibniz-Institut für Astrophysik Potsdam
CCD	Charge-Coupled Device
CME	Coronal Mass Ejection
DAVE	Differential Affine Velocity Estimator
DN	Data Number
EIT	Extrem Ultraviolet Imaging Telescope
EFR	Emerging Flux Region
EUV	Extrem Ultra-Violet
EUVI	Extrem Ultraviolet Imager
EVE	Extreme ultraviolet Variability Experiment
FFT	Fast Fourier Transform
FITS	Flexible Image Transport System
FOV	Field-of-View
FT	Feature Tracking
FWHM	Full-Width-at-Half-Maximum
Hi-C	Highresolution Coronal Imager
HMI	Helioseismic and Magnetic Imager
IDL	Interactive Data Language
JPEG	Joint Photospheric Experts Group
JSOC	Joint SDO Operation Center
K	Kelvin
KSC	Kennedy Space Center
LMSAL	Lockheed Martin Solar and Astrophysics Laboratory
LCT	Local Correlation Tracking
LOS	Line-of-Sight
LWS	Living with a Star
MDI	Michelson Doppler Imager
MHD	Magnetohydrodynamics
MK	Million Kelvin
Mm	Megameter
NAFE	Noise Adaptive Fuzzy Equalization
NASA	National Aeronautics and Space Administration
NAVE	Non-Linear Affine Velocity Estimator
NOAA	National Ocianic and Atmospheric Administration
NSO	National Solar Observatory
PIL	Polarity-Inversion-Line
PROBA2	PRoject for OnBoard Autonomy 2
ROI	Region-of-Interest

SDO Solar Dynamics Observatory
SDP Science-Data Processing
SoHO Solar and Heliospheric Observatory
SSD Sum-of-Squared Differences
SSM Solar Maximum Mission
SSW SolarSoft
STEREO Solar TErrestrial RElations Observatory
SWAP Sun Watcher using APS detectors and image Processing

TRACE Transition Region and Coronal Explorer

US United States
UT Universal Time
UV Ultra Violet

VTT Vacuum Tower Telescope

WWW World Wide Web

Selbstständigkeitserklärung

Hiermit erkläre ich, dass ich diese Arbeit selbständig verfasst und keine anderen als die von mir angegebenen Hilfsmittel und Quellen genutzt habe.

Andrea Diercke	Ort, Datum